Large-Eddy Boundary Layer Entrainment

D. C. LEWELLEN AND W. S. LEWELLEN

Department of Mechanical and Aerospace Engineering, West Virginia University, Morgantown, West Virginia

(Manuscript received 28 July 1997, in final form 12 January 1998)

ABSTRACT

A series of large-eddy simulations have been performed to explore boundary layer entrainment under conditions of a strongly capped inversion layer with the boundary layer dynamics driven dominantly by buoyant forcing. Different conditions explored include cloud-top cooling versus surface heating, smoke clouds versus water clouds, variations in cooling height and optical depth of longwave radiation, degree of cloud-top evaporative instability, and modest wind shear. Boundary layer entrainment involves transport and mixing over a full range of length scales, as warm fluid from the region of the capping inversion is first transported into the boundary layer and then mixed throughout. While entrainment is often viewed as the small-scale process of capturing warm fluid from the inversion into the top of the boundary layer, this need not be the physics that ultimately determines the entrainment rate. In these simulations the authors find instead that the entrainment rate is often limited by the boundary layer–scale eddy transport and is therefore surprisingly insensitive to the smaller scales of mixing near the inversion. The fraction of buoyant energy production available to drive large eddies that is lost to entrainment rather than dissipation was found to be nearly constant over a wide range of simulation conditions, with no apparent fundamental difference between top- versus bottom-driven or cloudy versus clear boundary layers. In addition, it is found that for quasi-steady boundary layers with dynamics driven by cloud-top cooling there is an effective upper limit on the entrainment rate for which the boundary layer dynamics just remains coupled, which is often approached when the cloud top is evaporatively unstable.

1. Introduction

Boundary layer entrainment is a critical, much studied, but still relatively poorly understood element of planetary boundary layer dynamics. While cloud-top entrainment velocities are typically much smaller than their counterparts within the boundary layer (~1%), the temperature and humidity fluxes they give rise to are not. These entrainment fluxes can strongly affect the dynamics and cloud structures within the boundary layer; the resulting feedback can further increase these effects.

An understanding of entrainment is complicated by the many dynamical forces that can contribute—for example, surface sensible and latent heating, cloud-top radiative or evaporative cooling, wind shear, or any combination of these, often changing in time. Moreover, the entrainment mixing process involves a full range of length scales; small-scale mixing across the inversion, perhaps intermediate-scale mixing in a region below the inversion, capture and transport of this fluid throughout the boundary layer by boundary layer–scale eddies, and finally a mixing cascade back down to small scales. As a consequence there are many different pictures that have been proposed to explain the entrainment process. Most studies have emphasized the importance of small-scale mixing effects near the inversion and the particular mechanisms involved—for example, Kelvin–Helmholtz wave breaking, plume ''splashing,'' the entrainment of thin ribbons, etc.—but this need not be the scale of physics that ultimately determines the entrainment rate, just as dissipation is ultimately a small-scale viscous phenomena but the overall dissipation rate in the flow is often determined by large-scale energetics. For given dynamical conditions it is unclear a priori which step or steps in the entrainment mixing process are the limiting ones determining the overall entrainment rate. In a quasi-steady boundary layer the entrained temperature and humidity fluxes must be carried uniformly throughout the boundary layer—from the inversion to the surface. The mechanisms operating on different length scales to carry this flux will necessarily adjust to be consistent with one another. If small-scale mixing at the inversion initially transmits the entrained fluxes at a greater rate than the large-scale eddies, then the inversion region will grow and the gradients there weaken, thereby reducing the small-scale flux transport while potentially increasing the large scale. Conversely, if the large-eddy transport initially exceeds the small scale then this will sharpen the inversion gradients leading to increased small-scale transport. Which scale of dynamics ultimately controls the overall entrainment rate is

Corresponding author address: W. S. Lewellen, MAE Dept., WVU, P.O. Box 6106, Morgantown, WV 26506.
E-mail: slewellen@cemr.wvu.edu

largely a question of whether the small-scale dynamics adjusts to the large scale or vice versa.

In this work we present results of large-eddy simulations of quasi-steady, strongly capped, buoyantly driven boundary layers with and without clouds. We clearly cannot resolve all mixing scales in any realistic atmospheric flow in a large-eddy simulation. If, for given dynamics, small-scale mixing in the inversion region turns out to be the limiting process determining the entrainment rate then the entrainment rate found from a large-eddy simulation will likely depend strongly on grid resolution and subgrid modeling near the inversion, and the results will not be particularly useful. Accordingly, we focus on the role of large (generally boundary layer scale) eddies in the entrainment process, and take as our working assumption that this scale of transport is the limiting stage determining the overall entrainment rate, at least within some dynamical regimes. This is plausible since the small eddies can adjust on a faster timescale than the large eddies, making it more natural for the small-eddy dynamics to adjust to the large-eddy dynamics rather than vice versa, in equilibrating the different entrainment rates. We have tested this assumption with simulations as best we can; the results (including a sampling presented below) lend support to its validity in many cases. We find as well that while smaller eddies (e.g., cloud scale or below) affect the entrainment rate in some cases, the larger-scale transport still plays a crucial role that allows us to determine useful bounds on the observed entrainment rate.

In section 2 we present an entrainment parameterization motivated by this point of view, which we will use in presenting our large-eddy simulation (LES) results. It is closely related to the flux partitioning parameterization of Stage and Businger (1981a,b). A brief overview of our LES model is given in section 3. In section 4 we consider simulations driven by either cloud-top radiative cooling or surface heating, but without any condensation or evaporation. This set includes several variations of the 1995 GEWEX Cloud System Studies (GCSS) ''smoke cloud'' intercomparison case (Bretherton et al. 1998, hereafter BR98), which motivated much of the work in the present study, and is discussed in other recent entrainment studies [e.g., Lock (1996) and Stevens and Bretherton (1998, hereafter SB98)]. Section 5 presents results from simulations including phase change energetics. Section 6 concludes with some summary discussion and suggestions for future work.

2. Large-eddy entrainment efficiency

We restrict our attention to quasi-steady boundary layer dynamics—that is, situations in which any changes in the underlying forcing or character of the horizontal mean profiles within the boundary layer occur on timescales long compared to the dynamical eddy timescales. In this limit the horizontal mean flux profiles of conserved variables are linear within the boundary layer and different scale eddy dynamics have all adjusted to one another. Further restricting attention to buoyantly driven dynamics, we find a simple global energy balance: the system finds an equilibrium in which the integrated buoyancy flux (i.e., buoyant energy production) equals the integrated dissipation. In this balance the energetic cost of entrainment is encoded in its effects on the buoyancy flux, which is reduced by the work required to mix warm fluid from the inversion region down and throughout the boundary layer. Accordingly, we define an entrainment efficiency for the boundary layer–scale eddy part of the entrainment process:

$$\eta_E \equiv (P_{NE} - P)/P_{NE}, \tag{1a}$$

where P represents the production rate of boundary layer–scale eddy kinetic energy and P_{NE} the production rate that would exist were there no large eddy entrainment. For buoyantly driven dynamics we generally approximate this as

$$\eta_E = \int (\overline{w'B'}_{NE} - \overline{w'B'})\, dz \Big/ \int (\overline{w'B'}_{NE})\, dz, \tag{1b}$$

where $\overline{w'B'}$ is the actual mean buoyancy flux profile, and $\overline{w'B'}_{NE}$ is that which would arise if there were no entrainment. Thus η_E represents the fraction of the total available buoyant energy production that is removed by entrainment rather than dissipation. Equation (1b) is a good approximation to (1a) as long as the fraction of the total buoyant energy production that goes toward driving boundary layer–scale eddies is not strongly affected by the presence of entrainment [i.e., $P/\int(\overline{w'B'})\, dz \approx P_{NE}/\int(\overline{w'B'})_{NE}\, dz$].

We can estimate $\overline{w'B'}_{NE}$ by using the assumption of linear flux profiles for the conserved total water $\overline{w'q'}$, and thermal (i.e., radiation plus liquid potential temperature, $\mathcal{F}$) fluxes. For example, given a cloud-top radiative cooling flux profile $F_{rad}(z)$; that portion of the radiative flux jump driving the boundary layer dynamics, $\alpha\Delta F_{rad}$; and surface fluxes of liquid potential temperature and total water, $\overline{w'\theta_l'}_{surf}$ and $\overline{w'q'}_{surf}$ (all assumed known), we have within the boundary layer:

$$\begin{aligned}\mathcal{F}_{NE}(z) &\equiv \overline{w'\theta_l'}_{NE} + F_{rad} \\ &= (1 - z/z_h)\overline{w'\theta_l'}_{surf} + (z/z_h)\alpha\Delta F_{rad}\end{aligned} \tag{2a}$$

and

$$\overline{w'q'}_{NE}(z) = (1 - z/z_h)\overline{w'q'}_{surf}. \tag{2b}$$

As a practical definition for our simulations, we have taken the ''no-entrainment'' mixed-layer height z_h to be the height of the peak minimum $\overline{w'\theta_l'}$. Generally this can be considered as the full extent of the boundary layer, though we consider some cases driven by radiative cooling located well below the temperature inversion where this is not the case.

Using (2) the no-entrainment buoyancy flux can be approximated by

$$\overline{w'B'}_{\rm NE} = (g/\theta_0)\overline{w'\theta'_v}_{\rm NE} = (g/\theta_0)(X_1\overline{w'\theta'_l}_{\rm NE} + X_2\overline{w'q'}_{\rm NE}), \quad (3a)$$

or, equivalently,

$$\overline{w'B'}_{\rm NE} = \overline{w'B'} + (g/\theta_0) \times [X_1(\mathcal{F}_{\rm NE} - \mathcal{F}) + X_2(\overline{w'q'}_{\rm NE} - \overline{w'q'})], \quad (3b)$$

where X_1 and X_2 depend on the liquid water contribution to the buoyancy flux from the two conserved variable fluxes. Except where explicitly noted we follow Sommeria and Deardorff (1977) and approximate:

$$X_1(z) = 1 - \alpha_s r(L/c_p - 1.61T(T/\theta))/(1 + \alpha_s L/c_p)$$

and

$$X_2(z) = 0.61T + r((\theta/T)L/c_p - 1.61T)(1 + \alpha_s L/c_p), \quad (4)$$

where r is the mean cloud fraction vertical profile, α_s is the slope of the saturated humidity with respect to temperature at constant $T_l \equiv \theta_l T/\theta$, L is the latent heat of vaporization, c_p is the specific heat of the mixture at constant pressure, T is the temperature, θ is the potential temperature, and θ_l is the liquid potential temperature. The form for the flux given in (3b) helps to limit the sensitivity to the modeling assumptions in (4) by modeling only the flux differences between the measured and no-entrainment cases rather than the (generally larger) no-entrainment fluxes themselves as in (3a).

In (2a) we have included only that part of the cloud-top radiative cooling flux jump that buoyantly drives large-scale dynamics: $\alpha\Delta F_{\rm rad} = \Delta F_{\rm rad} - \Delta\mathcal{F}_{\rm dc}$. In general a portion of the radiative cooling occurs in the warm inversion region itself, $\Delta\mathcal{F}_{\rm dc}$, directly cooling this fluid without driving buoyant dynamics. There is no consensus in the literature on how to treat this ''direct cooling'' portion of the radiation flux in parameterizing entrainment effects. Here we follow McEwan and Paltridge (1976), in separating this entrainment mechanism from that due to turbulent mixing. From the viewpoint of the present work this is clear: $\eta_{\rm E}$ in (1a) measures the entrainment efficiency as governed by boundary layer–scale eddy dynamics—that is, that fraction of what would be positive buoyancy flux that is ultimately lost through large-scale entrainment mixing. The direct cooling portion of $F_{\rm rad}$ does not give rise to any positive buoyancy flux and is considered separately; it represents 100% efficient entrainment in the sense that all of this portion of $F_{\rm rad}$ cools warm fluid in the inversion or above without any loss to dissipation. Given our focus on large-eddy entrainment, we will not try to compute $\Delta\mathcal{F}_{\rm dc}$ from first principles but simply diagnose its magnitude in each case from the simulation results. Intuitively we expect $\Delta\mathcal{F}_{\rm dc}$ to be that portion of $F_{\rm rad}$ above some height in the inversion region, but we choose not to measure it in this fashion because we do not know precisely which height is appropriate and, given the sharp gradient of $F_{\rm rad}$ in the inversion region, the result would be highly sensitive to this choice. Instead, as illustrated in Fig. 1, we first approximate the total entrained thermal flux into the boundary layer, $\Delta\mathcal{F}$, as the jump implied from extending the slope of the thermal flux profile to the height, z_h, of the peak negative $\overline{w'\theta'_l}$ flux. We partition this total entrained flux into two pieces: that due to turbulent mixing (approximated as the magnitude of the peak negative $\overline{w'\theta'_l}$ flux), and the remainder, which we take as our approximation to $\Delta\mathcal{F}_{\rm dc}$. This measure of direct cooling behaves correctly in the two extreme limits of all cooling within the inversion (for which $\Delta\mathcal{F}$ equals the full radiative flux jump and $\overline{w'\theta'_l}_{\rm min} = 0$) or all cooling below the inversion (for which $\Delta\mathcal{F} = \overline{w'\theta'_l}_{\rm min}$); there is a systematic uncertainty as to how well this measure works in between. Note that the magnitude of $\Delta\mathcal{F}_{\rm dc}$ is limited somewhat by the dynamics in the quasi-steady case: direct cooling in the inversion region tends to decrease the inversion thickness, which in turn decreases the fraction of direct cooling itself.

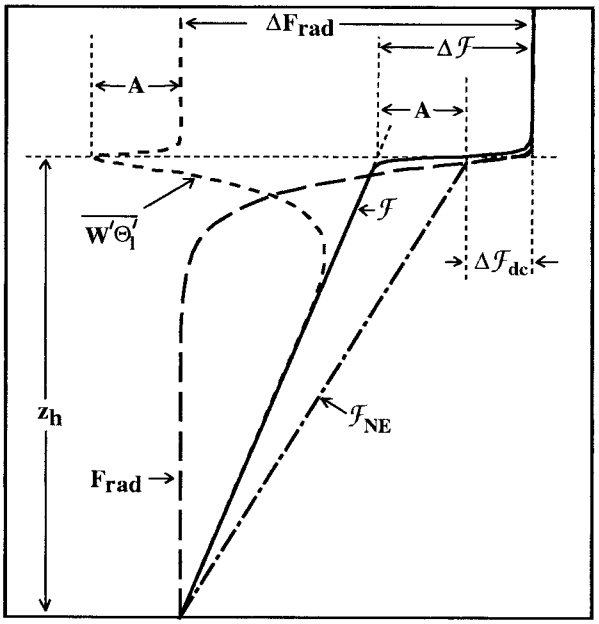

FIG. 1. Approximate measure of the direct cooling portion, $\Delta\mathcal{F}_{\rm dc}$, of the total radiative flux jump, $\Delta F_{\rm rad}$, for a top-cooled boundary layer. The mean thermal flux, $\mathcal{F}$, is defined as the sum of the conserved temperature flux, $\overline{w'\theta'_l}$, and the radiation flux, $F_{\rm rad}$. Here $\Delta\mathcal{F}_{\rm dc}$ is taken as the difference between the magnitude of the thermal flux jump, $\Delta\mathcal{F}$, and the magnitude of the peak minimum temperature flux labeled A here. The thermal flux in the absence of large-scale turbulent entrainment, $\mathcal{F}_{\rm NE}$, is as defined in Eq. (2).

The differences between the actual and no-entrain-

ment fluxes for the conserved variables are the turbulent entrainment fluxes, given by the following equations for $z < z_h$,

$$\begin{aligned} \mathcal{F}_{\mathrm{NE}} - \mathcal{F} &= \overline{w'\theta'_l}_{\mathrm{NE}} - \overline{w'\theta'_l} \\ &= z/z_h(w_e\Delta\theta_1 - \Delta\mathcal{F}_{\mathrm{dc}}), \\ \overline{w'q'}_{\mathrm{NE}} - \overline{w'q'} &= z/z_h w_e \Delta q, \end{aligned} \tag{5}$$

where $\Delta\theta_l$ and Δq are the appropriate jumps across the inversion. In these parameterizations, the entrainment velocity itself, w_e, appears only in combinations representing the fluxes. This is appropriate if the feedback between the large-eddy dynamics and the entrainment in fact controls the entrainment rate, which is our working assumption. While details of the mean inversion structure such as the local temperature and humidity gradients, diffusion rates, etc., will strongly affect the small-scale-eddy dynamics in these regions, they will have little direct affect on the boundary layer–scale dynamics. In the limit of strong capping, the dominant effects of the inversion structure and entrainment itself on the boundary layer–scale eddy dynamics should be through the entrainment fluxes alone.

In the case of dry surface-driven convection in the approximation of a zeroth-order mixed-layer model, (1b) reduces to the familiar ratio of the negative temperature flux at the top of the boundary layer to the surface flux. Several generalizations of this basic dimensionless entrainment measure have been proposed for more complicated boundary layer dynamics, some close in spirit to (1a), others much less so. Aside from some details of application, the approximation of (1a) given in (1b)–(4) is in essence the parameterization scheme proposed by Stage and Businger (1981a,b). We have provided a somewhat different motivation for this form; in particular we have not made any assumptions about the possible independence of the various contributions to the buoyancy flux, which are sometimes (e.g., Randall 1984; Moeng et al. 1992) involved in discussing Stage and Businger's parameterization. Nonetheless, in most cases to which we apply it, the practical form is the same. There are at least two general cases where the parameterization differs significantly enough to be worth noting, however. The first is the case in which there is more than one entrainment region. For example, given a cold surface we have entrainment of cold air from off the surface as well as warm air from the inversion region capping the boundary layer. In discussing this case, Stage and Businger sum the two entrainment cost contributions. In defining the ''no entrainment'' production terms in (1), we consider the two entrainment processes independently. As will be shown in section 4 this is necessary for agreement with our LES model results.

Second, we differ with Stage and Businger's parameterization whenever the approximation leading from (1a) to (1b) breaks down, that is, when some additional physics drives small- or intermediate-scale eddies independently of the boundary layer–scale ones. Consider three simple thought experiments. First, consider a boundary layer convectively driven with any combination of top cooling and surface heating. We add to this, somewhere well above the surface but well below the inversion, a layer of modest thickness (compared to z_i), which we cool at the top and heat at the bottom. We can thereby produce vigorous buoyancy production, which does not drive boundary layer–scale eddies; we would not include this energy production in evaluating (1a). Next consider a boundary layer convectively driven from the surface to which we again add a buoyantly driven layer of modest thickness, placed now at the top of the boundary layer. The added buoyant production again drives intermediate, rather than boundary layer–scale, eddies which in this case participate in the entrainment dynamics at the top of the domain. The transport of the entrained fluxes from just below the added layer to the surface is again the responsibility of the boundary layer–scale eddies; from their perspective the added mixing layer merely thickens the inversion region. We again would not include the smaller-scale buoyancy production in (1a), and the large-eddy entrainment cost would be computed from the bottom of the now thickened inversion region down to the surface. Finally, we consider this same case but with the boundary layer–scale dynamics driven by radiative top cooling rather than surface heating. The added small-scale eddies now have a much more significant affect on the boundary layer–scale eddies than just thickening the inversion region. They can directly mix warm entrained fluid with radiatively cooled fluid just below the inversion, robbing the large eddies of some of their buoyant driving potential in analogous fashion to the direct cooling entrainment discussed above. In evaluating (1a) we should in principle only include that fraction of buoyant energy production that remains (after the small-scale mixing) to drive boundary layer–scale eddies. In practice, this may be difficult or impossible to determine, but some useful limits on the entrainment can be determined nonetheless. We will consider this further in section 5 when we will encounter versions of these latter two thought experiments in boundary layers with cloud tops which are evaporatively unstable.

Other popular entrainment parameterizations are less natural from a large-eddy entrainment point of view. For example, Kraus and Schaller (1978) consider the ratio of the negative part of the buoyancy flux profile to the positive part:

$$\begin{aligned} k^2 = &-(\text{Integral of negative } \overline{w'B'}) \\ &\div (\text{Integral of positive } \overline{w'B'}). \end{aligned} \tag{6}$$

This is similar to (1) in that it involves the ratio of a boundary layer–integrated estimate of the entrainment cost to energy production. Equation (1) differs from (6) in including the energetic cost of the entrainment flux

throughout the boundary layer, even where $\overline{w'B'}$ is positive. The difference is most striking for dynamics driven by cloud-top radiative cooling; if the cooling layer is thin then the negative buoyancy flux integral in (6) becomes very small, while the entrainment cost as measured by the numerator in (1) remains sizable.

Schubert (1976) considers a linear interpolation between the minimum and maximum entrainment hypotheses of Lilly (1968), which involves then the ratio of the minimum in the buoyancy flux profile to the layer-averaged value:

$$\frac{2k}{(1-k)} = -\overline{w'B'}_{\min} \Big/ \left[\left(\frac{1}{z_i}\right)\int_0^{z_i} \overline{w'B'}\, dz\right]. \quad (7)$$

This is again a flux-based entrainment measure, but with the entrainment cost tied to a single point of the profile (the minimum) and without considering the relation of $\overline{w'B'}(z)$ to the imposed boundary layer forcing.

Finally there are the familiar Richardson number parameterizations, as suggested by Turner (1973), where the entrainment cost is measured entirely by a buoyancy jump across the inversion, ΔB, as would be appropriate if small-scale dynamics at the inversion controlled the entrainment rate. For example,

$$w_e/w^* \equiv A(\mathrm{Ri})^a \quad \text{with} \quad \mathrm{Ri} \equiv \Delta B z_i/w^{*2} \quad \text{and}$$

$$w^{*3} = 2.5\int \overline{w'B'}\, dz. \quad (8)$$

If $a = -1$ (which is at least consistent with much, if not all, of the experimental data), then the entrainment enters the parameterization again only through the flux combination, $w_e\Delta B$. We have argued above that the dependence on the entrainment fluxes alone is to be expected if boundary layer–scale eddy dynamics determines the entrainment rate; it need not be so if small-scale dynamics governs.[1] For cloudy boundary layers it is not clear how one should define ΔB in (8); the estimated energy cost of moving a parcel of fluid across the inversion depends on what mixing assumption is made (e.g., MacVean and Mason 1990). For simplicity we take $\Delta B = (g/\theta_0)\Delta\theta_v$ for "A" values that are quoted in section 5.

In the simple case where the buoyancy flux is linear within the boundary layer [and $a = -1$ in (8)] all of the parameterizations are effectively equivalent (except in philosophy). For example, in the dry surface-driven zeroth-order jump case,

$$\eta_E = -\overline{w'B'}(z_i)/\overline{w'B'}(0) = k = A/(A + 0.8). \quad (9)$$

It is only for nonlinear buoyancy fluxes that the dimensionless entrainment measures in (1), (6), (7), and (8) become physically distinct.

In cases where large-eddy energetics control the entrainment rate, η_E should prove a useful dimensionless entrainment measure; however, there is no reason, a priori, that it need be precisely constant. We expect (and support with LES results below) that when the large-eddy dynamics is broadly similar η_E should be roughly constant. On the other hand, as noted above, the large-scale entrainment energetics represents a competition between the energy losses due to entrainment and dissipation. If large-eddy dynamics set the entrainment rate, then the dissipation dynamics will necessarily play a role and any significant differences in dissipation dynamics could alter the entrainment efficiency.

3. LES model review

The LES model used is the same as that used by Lewellen et al. (1996). Its basic features were described by Sykes and Henn (1989) with the cloud dynamics given by Sykes et al. (1990). It is a fully three-dimensional, unsteady, finite-difference implementation of the incompressible Navier–Stokes equations in the Boussinesq approximation, second-order accurate in space and time. The piecewise parabolic model (PPM) algorithm is used in the advection of temperature and humidity to allow sharp gradients in the inversion region to be advected without spurious overshoots and undershoots or excessive numerical diffusion. The Poisson equation for the pressure required to implement continuity is solved directly using fast Fourier transforms in the horizontal directions and matrix inversion in the vertical. The grid spacing is uniform in the horizontal directions, and the boundary conditions periodic. We employ a stretched grid spacing in the vertical to permit improved resolution around the inversion and near the surface. Staggered grids are used for different field variables. For the simulations presented in this work, the surface temperature and humidity fluxes are specified, and the surface is very smooth (roughness length equal to 10^{-16} m). The subgrid closure utilizes a quasi-equilibrium, second-order turbulence closure scheme with the maximum turbulence length scale related to the numerical grid length. The model includes the possibility for partial cloudiness within an individual grid cell to allow us to deal with small-scale mixing between cloudy and clear air. The subgrid cloudiness parameterization is that given for Gaussian probability distribution functions (Sommeria and Deardorff 1977; Mellor 1977). We carry the saturation variance as an additional prognostic variable consistent with our second-order closure scheme.

Note that one change in numerics was implemented specifically for the present work. In studying entrainment any possible numerical energy sources in the vicinity of the inversion are a concern. We carry vertical velocity and temperature on grids staggered with respect to each other, so that the latter must be interpolated to

[1] If A is independent of ΔB, then $a = -1$ also follows from (8) in the strongly capped limit under the weaker assumptions that the entrainment flux combination $w_e\Delta B$ is both finite (which it must be) and nonzero (which is reasonable) in the limit $\Delta B \to$ large.

the same grid as the former to implement the buoyant forcing in the vertical momentum equation. This interpolation should be consistent with the advection scheme used for the temperature (PPM in our case) in order to avoid a possible weak violation of energy conservation.[2] Accordingly we use the same PPM scheme for the interpolation as for the temperature advection; however, this creates potential difficulties in the inversion region itself, where the temperature gradients are strong and the vertical velocity near zero. The PPM interpolation scheme (being essentially an upwind algorithm) can lead to a discontinuity in the interpolated temperature as w flips sign. This can lead to an oscillatory instability (of bounded amplitude) with w flipping sign between every time step. To avoid this we smoothly pass between the PPM interpolation (for vertical velocity of magnitude above some cutoff) and a simple centered interpolation (for $w = 0$) to avoid any discontinuity. As a practical matter we have found these difficulties to be of negligible importance for the fine vertical grid spacings (generally 5 m) employed in the present work, but of significance for coarser vertical spacing, where the treatment described proved beneficial.

4. LES results for dry convection

a. Radiatively cooled smoke cloud

We begin with the radiative ''smoke cloud'' case from the second GCSS model intercomparison study held in De Bilt, the Netherlands, in 1995. This case simulates a boundary layer driven by cloud-top radiative cooling with all evaporation and condensation effects removed. The domain is 3.2 km $\times$ 3.2 $\times$ 1.5 km; the initial boundary layer height was 700 m with an initial temperature jump across the inversion of 7 K. The smoke cloud has an optical depth of 44 m (defined as the length over which a fraction 1/e of incoming radiation would be attenuated in the undiluted smoke cloud), and radiatively cools at a fixed rate of 60 W m^{-2} with ρ^c_p taken as 1148 J K^{-1}m^{-3}. We refer the reader to BR97 for further details of this case and a summary of the results from different LES models. We have considered several variations of this basic case including differing resolution, subgrid model, optical depth, cooling height, and wind shear. Two changes were made generally. One conclusion of the intercomparison was that a relatively high vertical resolution (of order 10 m or better) in the inversion region is required to obtain consistent entrainment results between different LES models. Accordingly we employ 5-m vertical resolution in the vicinity of the inversion for all of the results presented here (except where explicitly noted), rather than the standard 25 m used in the intercomparison. We also ran each simulation for long enough to obtain quasi-steady results for at least two separate hour periods (often using the flow field of a closely related run for initial conditions to speed up the approach to equilibrium). The comparison case presented in BR98 was initialized with a random perturbation of a quiescent field with results gathered between simulation hours 2 and 3.

Some of the results from the smoke cloud runs are summarized in Table A1 in appendix A; we will highlight a few salient points here. Figure 2 includes a sample of the averaged mean vertical profiles for simulations with different horizontal resolution. The averaging period chosen is from simulated hours 4–5 for simulations 12, 14, and 15, and hours 2–3 for simulations 10 and 11 (which were initialized with the fields from simulations 14 and 12, respectively, at 2 h); thus the simulated age is the same for each case. The profiles in Fig. 2 are remarkably insensitive to the variation in horizontal resolution, which covers a full order of magnitude from 320 m to 32 m. This is found for the hour average preceding that in Fig. 2 as well. Given that the dynamics are basically steady in time and the radiation flux profile is fixed, the basic *shapes* of the flux profiles in Fig. 2 are also fixed, with only a single parameter depending on the entrainment rate (e.g., the jump in the thermal flux profile) free to vary. The entrainment efficiency is plotted directly for these cases in Fig. 3; the efficiencies derived from at least two different hour averaging periods are included to give some rough measure of the statistical uncertainty in the data. The results in Figs. 2 and 3 strongly support (and indeed helped motivate) the hypothesis that the boundary layer–scale eddy dynamics is controlling the entrainment rate in this radiatively cooled smoke cloud simulation. Changing the horizontal resolution strongly affects any numerical diffusion that may be present, as well as changing the relative importance of the subgrid modeling. On the other hand the basic dynamics of large boundary layer–scale rolls or plumes is roughly captured and the temperature flux is dominantly resolved (as opposed to subgrid) even in the coarse grid simulations. The resolved dynamics appears to be key: when we use coarse enough resolution in our model so that all of the dynamics is modeled in the subgrid (simulation 16), the entrainment velocity is decreased by a factor of 3, and η_E by a factor of 4. We have found the entrainment rate to be relatively insensitive to changes in horizontal grid resolution for many other types of boundary layer dynamics (as will be shown below), but none to the same degree as displayed in Fig. 2. This suggests that some detailed balance which we do not yet understand involving the resolved buoyant dynamics (and perhaps the direct cooling in the inversion) is responsible for the precise level of insensitivity in Fig. 2.

Table A1 includes results from simulations with varying vertical resolution in the inversion region, simulations 21–24, which should be compared with 12. We find no significant difference between the simulations

[2] We would like to acknowledge useful discussions with Ian Sykes and Malcolm MacVean regarding this point.

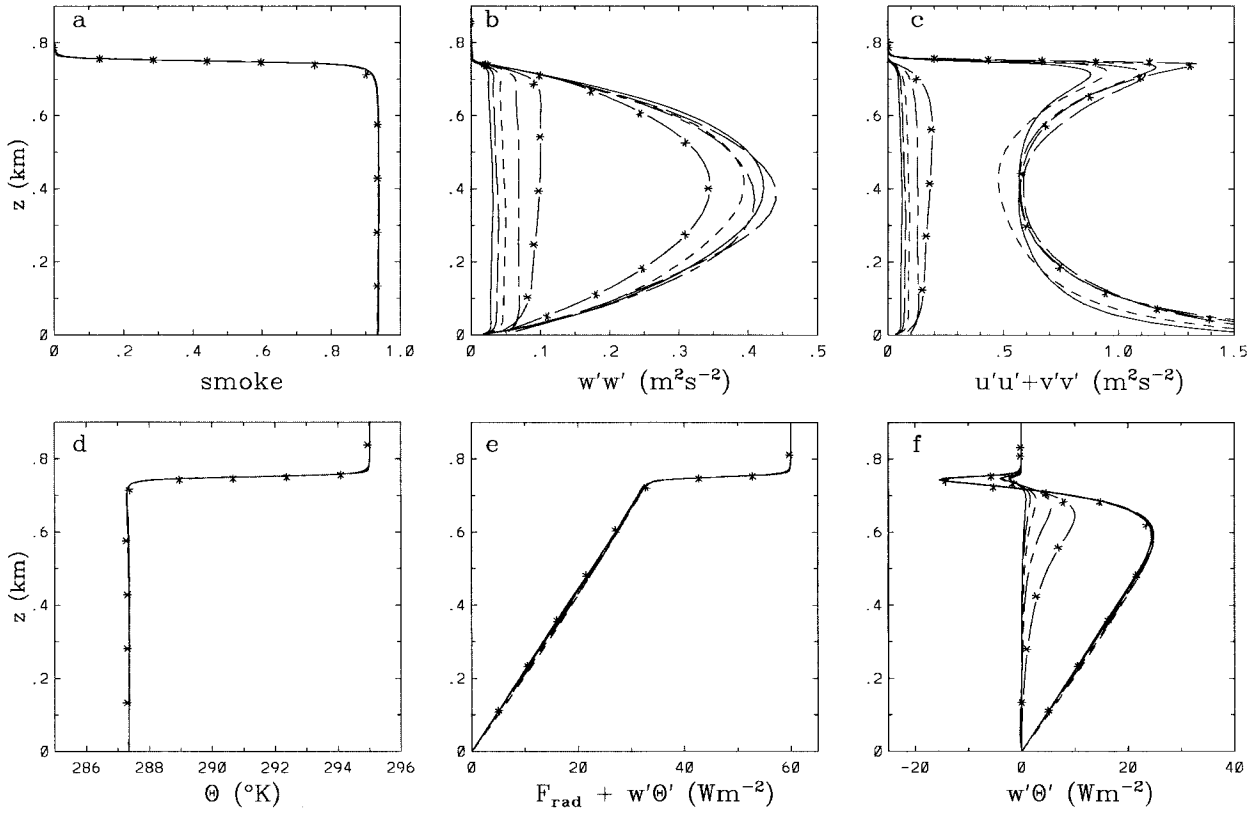

FIG. 2. Influence of horizontal resolution on hour-averaged, mean statistics from simulations of a radiatively cooled dry boundary layer. (a) Smoke concentration, (b) vertical velocity variance (total and subgrid), (c) horizontal velocity variance (total and subgrid), (d) potential temperature, (e) thermal flux, and (f) potential temperature flux (total and subgrid). Horizontal resolutions $\Delta x = 32, 50, 80, 160, 320$ m for simulations 11, 10, 12, 14, 15, respectively, are indicated by the solid, long-dashed, short-dashed, long–short dashed, and starred lines, respectively.

with $\Delta z = 1.25$, 2.5, and 5 m. As Δz is increased to 10 m (and to a much greater extent at 20 m), the inversion gradient cannot be maintained as sharply and so weakens; at the same time the total entrainment flux is modestly increased. The increased entrainment flux is probably due entirely to an increase in the portion of the radiative cooling occurring within the inversion (the direct cooling), due to the thicker inversion region. The large-eddy entrainment efficiency, η_E (defined with the direct cooling entrainment contribution approximately removed), is fairly constant with increasing Δz (as seen in Fig. 4). We have included measurements from simulations with different horizontal resolution and at different times on the figure; the scatter again serving the role of rough error estimates for the data points.

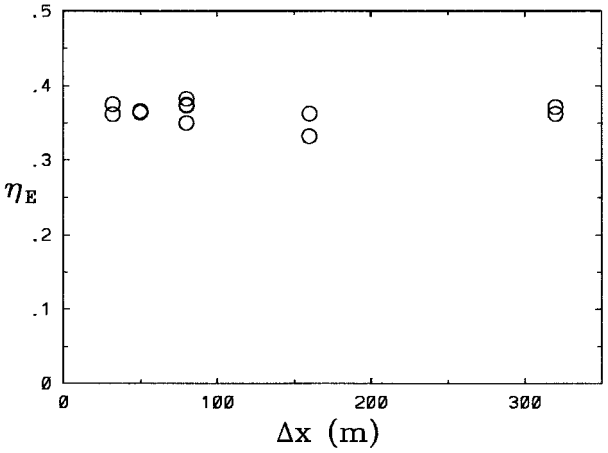

FIG. 3. Hour-averaged entrainment efficiencies as a function of horizontal resolution for radiatively cooled dry simulations.

Simulations 31–34 are of the standard radiatively cooled smoke cloud including the effects of varying some subgrid modeling parameters. In 31 and 32 we have increased the constant in our LES model that governs the subgrid turbulent scalar diffusion (increasing the Prandtl and Schmidt numbers) from their standard value of 0.75 to 50. This is large enough to effectively shut off the subgrid scalar diffusion in the simulation; it has little effect otherwise. Remarkably, the resolved temperature flux adjusts itself to make up for the lost subgrid contribution, leaving the entrainment effectively unchanged. This is true even for the simulation with coarse horizontal resolution, where the subgrid contri-

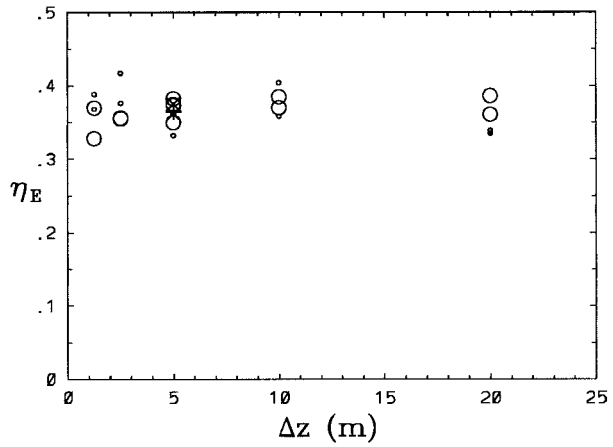

FIG. 4. Hour-averaged entrainment efficiencies as a function of vertical resolution for radiatively cooled dry simulations. Symbols indicate horizontal resolution: $\Delta x = 32$ m (×), 50 m (+), 80 m (large circle), and 160 m (small circle).

bution is forced to be significant (cf. run 32 vs 14 in Table A1).

In simulations 33 and 34 we have changed the ratio of the maximum subgrid turbulence length scale, Λ_{max}, to the horizontal grid spacing from our standard value for these runs of 0.3 to 0.2 and 0.4, respectively. The sensitivity to this change in subgrid modeling should be larger on the moderately coarse grid spacing ($\Delta x = 80$ m) employed than for a finer grid. In our LES model the subgrid turbulence length scale, Λ, is limited by the stratification in the inversion region, and by the distance to the surface at low altitude, so the major effects of changing Λ_{max} occur in the middle of the boundary layer. In this case we find a modest decrease in η_E as $\Lambda_{max}/\Delta x$ increases. This is consistent with the interpretation that any change that increases the dissipation (for a given level of turbulent kinetic energy) will reduce the entrainment. This interpretation is consistent with the results of simulation 35 for low Reynolds number as well (achieved by increasing the molecular viscosity), with the entrainment efficiency now markedly reduced.

In these variations of the GCSS smoke cloud case, we have found that the entrainment efficiency is remarkably insensitive to changes in resolution or subgrid modeling affecting small-scale dynamics, but is modified by changes that alter the dissipation rate of the boundary layer–scale eddies. These results support (and motivated) the interpretation that boundary layer–scale eddy dynamics determine the entrainment rate, at least in some dynamical regimes. Given the robustness of the

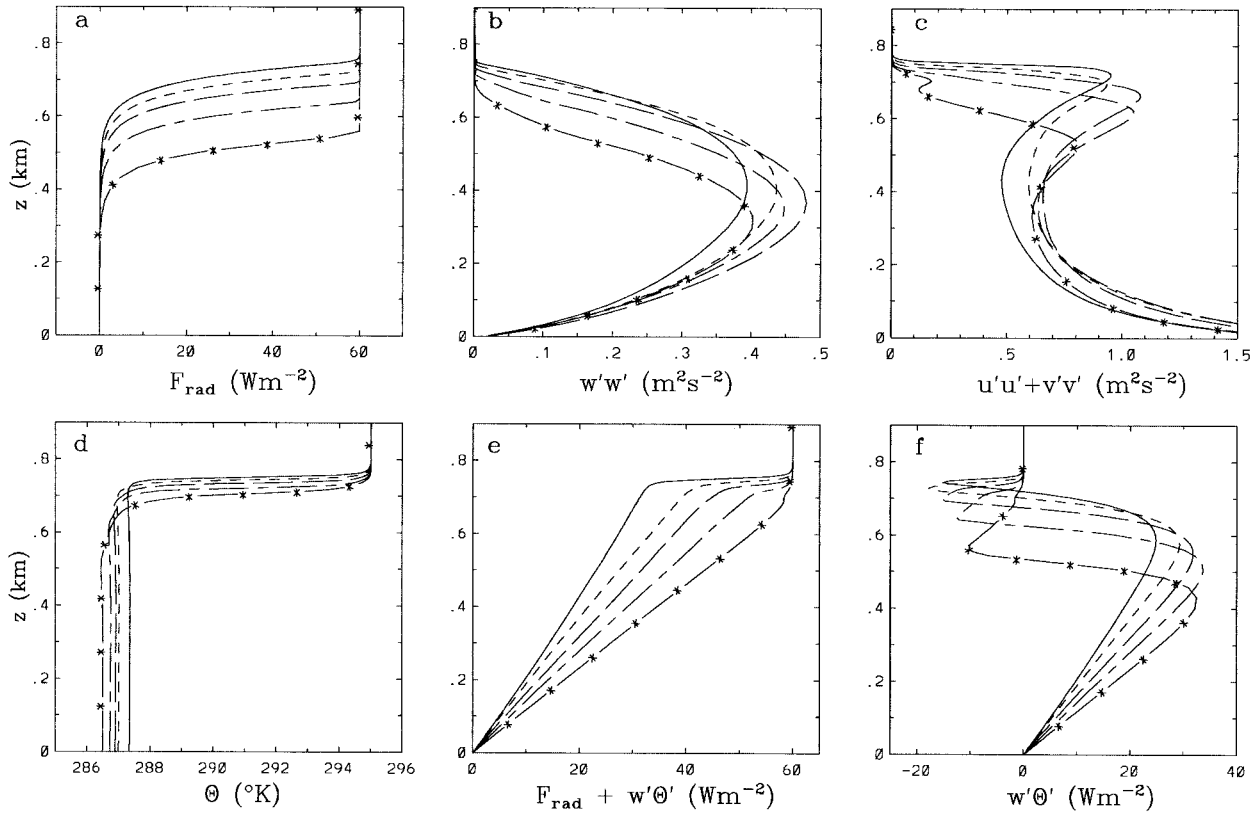

FIG. 5. Influence of a drop in cooling height on hour-averaged, mean statistics from simulations of a radiatively cooled dry boundary layer. (a) Radiation flux indicating drops in cooling height of $\Delta z = 0$, 20, 40, 80, and 160 m (simulations 13, 41, 42, 44, 45, respectively). (b)–(f) As in Fig. 2 except only total = resolved + subgrid shown for (b), (c), (f).

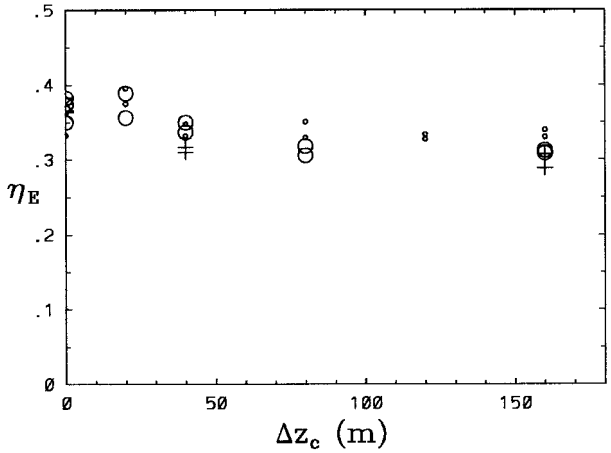

FIG. 6. Hour-averaged entrainment efficiencies as a function of cooling height for radiatively cooled dry simulations. Symbols indicate horizontal resolution: $\Delta x = 32$ m (×), 50 m (+), 80 m (large circle), and 160 m (small circle).

entrainment results presented above, the differences observed in the GCSS smoke cloud comparison study BR98, and the resolution study of SB98, deserve comment. We believe that the variations observed arise principally from three sources. First and foremost, the direct cooling contribution to entrainment is very sensitive to the temperature and smoke concentration gradients within the inversion and thus is quite sensitive to vertical grid resolution and the numerical scheme employed for the vertical advection of the scalar fields. Second, the time evolution of the buoyant energy production rate and the turbulent kinetic energy in the boundary layer starting from the initial randomly perturbed field includes a steady rise together with a damped oscillation (BR97). These features are still present during the 2–3-h averaging period employed for these results, and may be expected to vary somewhat from turbulent realization to realization or with different numerics and grid resolution. From our own simulations we estimate the uncertainties in these early time entrainment results to be of the order of 15%. Finally, our results suggest that any differences between LES models that affect the large-eddy dissipation dynamics (e.g., the dissipation rate for a given level of tke) can affect the measured entrainment rate. This is supported by the variation of η_E with $\Lambda_{max}/\Delta x$ presented above. These differences in dissipation modeling may vary with grid resolution differently in different LES models.

The same issues arise in comparing LES smoke cloud entrainment results with the most closely related laboratory experiments—those of McEwan and Paltridge (1976) and, more recently, Sayler and Breidenthal (1998). The latter find an apparent dependence of the entrainment rate on Prandtl number, and both find lower dimensionless entrainment rates [based on (8)] than the LES results in BR98. Expected differences in the direct cooling entrainment may account for the observed Prandtl number variation, though it is unclear how to accurately estimate the direct cooling portion of the entrainment in the laboratory experiments. Changes in the large-eddy dissipation dynamics may account for the lower laboratory entrainment measurements relative to the LES results. The laboratory experiments are for much lower Reynolds numbers than the simulations; we have already seen that this can dramatically reduce the entrainment rate. Moreover, the laboratory experiments are conducted in a tank that is relatively small in the sense that it can contain only a few boundary layer–scale eddies and these will necessarily interact with the side walls of the tank; this provides an additional source of energy dissipation from the large eddies, which, we expect, would further reduce the entrainment rate. We agree with Sayler and Breidenthal's argument that Reynolds number effects on the final mixing of entrained fluid will probably not affect the entrainment rate; however, the rate of energy lost from the large eddies *will* depend on Reynolds number (for low Re), which can change the entrainment rate by affecting the balance between the entrainment and dissipation energy sinks.

While we have found the entrainment rate in our simulations to be independent of the representation of subgrid transport in the inversion region, we have not, even in our highest-resolution cases, explicitly resolved all of this transport. In recent work, however, MacVean and colleagues have performed an extremely high-resolution simulation of the smoke cloud case (uniform 5-m grid spacing in all directions), which clearly resolves small-scale entrainment events in the inversion region (M. K. MacVean 1997, personal communication). The resulting average entrainment rate agrees well with that found in the highest-resolution simulations in the GCSS comparison and with those given here, providing strong additional support for our central premise.

We consider now two physical variations of the smoke cloud case. Figure 5 compares simulations in which the radiative flux profile has been computed from the smoke density as before but then the height of this cooling is lowered by a fixed amount (cases 41–46 and 13 in Table A1) Entrainment efficiencies from both higher and lower resolution for some of these cooling heights are given in Fig. 6. With even a small drop in cooling height the direct cooling portion of the radiation flux is dramatically reduced or eliminated and the total entrainment flux is reduced accordingly. When the cooling height has been dropped sufficiently, the inversion height (e.g., the height of the steepest temperature gradients) ceases to grow at all. A stable temperature gradient forms above the level of the radiative cooling, effectively lowering the capping inversion. Accordingly in computing η_E in Table A1 for these cases, we consider all of the mixing occurring above the top of the cooling flux profile (which coincides with the height of the peak negative temperature flux) to be entrainment. The entrainment efficiencies for these cases in Table A1 are fairly constant, both supporting the separation of the direct

cooling entrainment from the buoyantly driven entrainment, and demonstrating the relative insensitivity of the entrainment to the strength of the capping temperature gradient since those with significantly lowered cooling are capped by a weak gradient. The modest drop in η_E as the cooling profile is dropped may indicate that our prescription systematically underestimates the direct cooling portion of the entrainment, or may simply reflect the effects of the change in the large-eddy structure.

Note that once the cooling height has been dropped by 40 m or more, so that the direct cooling entrainment has been largely eliminated, the temperature flux profile is entirely fixed given the entrainment rate, radiation flux profile, and assumption of quasi-steady dynamics (giving a linear thermal flux profile). Conversely, given the radiation flux profile and quasi-steady dynamics in this case, the entrainment flux can be determined from any feature of the temperature flux profile—for example, its slope in the lower boundary layer, peak positive value, or peak negative value. Generally the latter measure of entrainment is used. We emphasize this simple point to demonstrate the fallacy in jumping to the conclusion that because one measures the entrainment using the negative flux peak, that the physics determining the entrainment rate is necessarily in this region of the boundary layer (typically right below the inversion). For the same reason, the ratio of subgrid peak negative temperature flux to resolved peak negative temperature flux, may be an entirely irrelevant measure of the relative importance of subgrid and resolved dynamics in determining the entrainment rate in a large-eddy simulation, although it is sometimes used as such.

In simulations 51–53 the radiative absorption coefficient of the smoke cloud is varied from its nominal value of 0.02 (e.g., in simulation 13). As the radiatively cooled layer deepens the direct cooling, available buoyant energy production, and buoyantly driven entrainment all decrease. The measured entrainment efficiency is again fairly constant with respect to the variation (Fig. 7).

Simulations 61–63 in Table A1 include jumps in horizontal velocity at the inversion of 1, 2, and 4 m s^{-1}, respectively. The turbulent energy production from wind shear in the first two cases is small compared with the buoyant production in the boundary layer ($<2\%$). The main effects of the shear are strictly local to the inversion region. As the shear is increased the subgrid energy production and diffusion increase as well, but for modest shear the entrainment efficiency appears to be unchanged. Of course, for large enough shear the shear instability would overcome the temperature stratification at the inversion and alter the dynamics. The case with velocity jump of 4 m s^{-1} is on the edge of this transition; at least in some local regions in the inversion the shear is large enough to lead to instability. The shear production increases to 7% of the buoyant energy production and the entrainment efficiency is increased to 0.44.

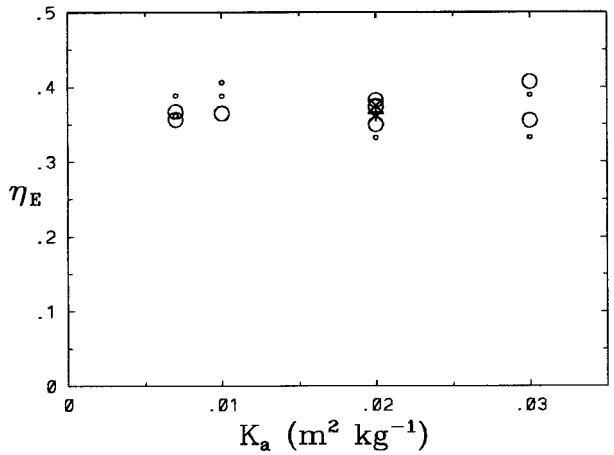

FIG. 7. Hour-averaged entrainment efficiencies as a function of optical absorption coefficient for radiatively cooled dry simulations. Symbols indicate horizontal resolution: $\Delta x = 32$ m (×), 50 m (+), 80 m (large circle), and 160 m (small circle).

b. *Surface-driven dry convection*

The radiatively cooled smoke cloud is complicated by the direct cooling effect, as well as by the different possible radiative flux distributions. Surface-driven dry convection, which we consider next, is simple in comparison, and has been the subject of many large eddy simulations [e.g., Moeng and Wyngaard 1984; Mason 1989; Schmidt and Schumann 1989). In this case both the driving and entraining temperature fluxes heat the boundary layer and tend to reduce the capping temperature jump. To get quasi-steady entrainment conditions one can either begin with a sufficiently large $\Delta\theta$ at the inversion or include a sizable lapse rate above the inversion so that $\Delta\theta$ is maintained as the inversion height grows. Sticking to the case of a tightly capped boundary layer, we take the former approach here so that the entrainment process is again unaware of conditions above the inversion. In simulation 70 the surface heat flux is 60 W m^{-2} and the initial $\Delta\theta$ across the inversion is 7 K as in the radiatively cooled smoke case. This simulation was initialized from a comparable simulation with coarser horizontal resolution and run for 3 h. Sample hour-averaged vertical profiles are given in Fig. 8. The entrainment efficiency is found to be quite close to that for the top-cooled smoke cloud ($\sim$0.3 vs $\sim$0.36). The modest reduction in efficiency may arise from changes in the large-eddy dynamics (e.g., the vertical velocity variance is peaked lower in the boundary layer for the surface-driven dynamics than for the top driven) or due to inaccuracy in removing the direct cooling contribution in the radiatively cooled case (which would be consistent with the closer agreement in η_E for the surface-driven case and the radiatively driven cases with the cooling height dropped).

In simulations 71–75 and 81–84, we employ an artifice to guarantee a tightly capped boundary layer and steady conditions in time, as well as to compare sim-

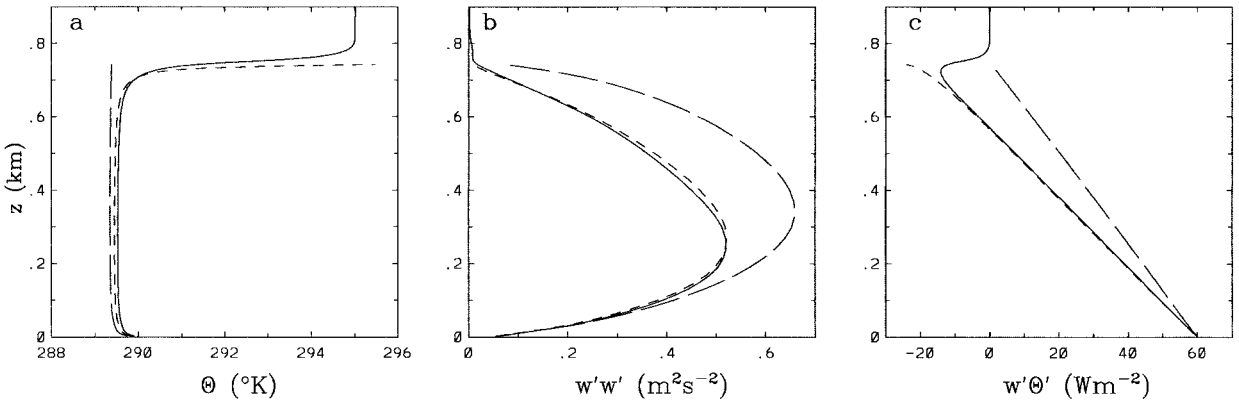

FIG. 8. Hour-averaged, mean statistics from simulations with surface-driven dry convection: Simulation 70 with inversion (solid line); 81 with top lid (long dashes); 71 with lid including negative heat flux (short dashes).

ulations with and without entrainment. We place a lid on the domain at 750-m height and consider the affect of varying the heat flux through this lid. Profiles from some of these simulations are also given in Fig. 8. For zero heat flux through the top lid there is no entrainment and all of the buoyant energy production driven by the surface heat flux is lost to dissipation (simulation 81). The dynamics is similar given a small negative top heat flux. This added heat is completely mixed through the boundary layer; the total dissipation rate is slightly reduced to balance the energy required to drive this negative contribution to the buoyancy flux. As the top negative heat flux is increased, at some point it energetically exceeds what can be mixed through the boundary layer, and a thin warm layer forms at the top of the domain with temperature increasing in time. Further increase in the top negative heat flux serves only to increase the rate of temperature increase in the thin top layer above the new inversion; the amount of heat flux entrained and mixed through the boundary layer is found to remain constant. The entrainment rate remains constant in time as well, even as the temperature jump at the new inversion grows with time. The measured η_E (e.g., for simulation 71) agrees with that found in 70 without the top lid. The dynamics in this case is steady in an ensemble average sense, allowing a statistically more accurate measurement of the entrainment flux. (The numerical requirements are also less expensive; there are no grid points above the inversion and the fine grid region around the inversion can be smaller since z_i does not grow.)

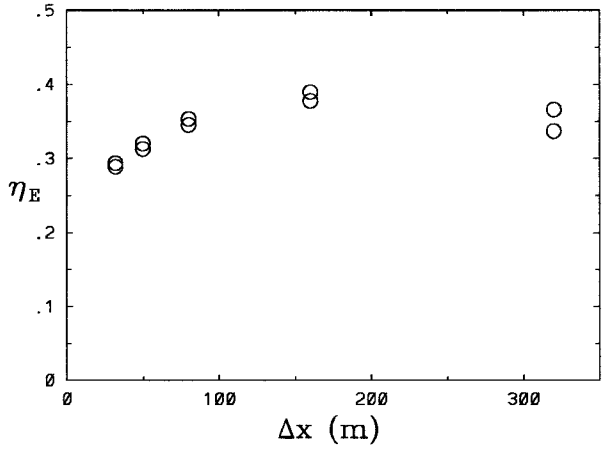

FIG. 9. Hour-averaged entrainment efficiencies as a function of horizontal resolution for surface-driven dry convection.

Note that as the inversion becomes less sharp (cf. 70 vs 71), η_E differs from the commonly used entrainment measure for dry surface driven convection, that is, the ratio of the peak negative heat flux to the surface heat flux, due to the rounding of the negative heat flux peak. This latter measure would imply (erroneously in this case) that the overall entrainment flux is strongly dependent on the inversion temperature gradient. This is the conclusion reached, for example, by Sorbjan (1996) from a series of LES of surface-driven convection, in which he varied the strength of the capping inversion. In η_E we are effectively measuring the rate of heat entrainment into the boundary layer from the rate of change of the boundary layer temperature (i.e., from the average slope of the heat flux in the boundary layer), together with the known surface flux and the conservation of total heat. This gives a more accurate measure of the total entrained heat flux than the magnitude of the negative heat flux peak when the inversion gradients are weak. By this measure Sorbjan's (relatively coarse grid) data is in fact consistent with the entrainment flux being insensitive to the inversion strength. This difference in measuring the entrainment efficiency is also, we believe, responsible for the difference between the value of 0.3 measured in our simulation and the value of 0.2–0.25, which is often quoted. In recent work Lock (1996) reaches this same conclusion, though with a slightly different parameterization, and finds as well similar entrainment rates in the radiatively cooled smoke cloud once the direct cooling entrainment is subtracted.

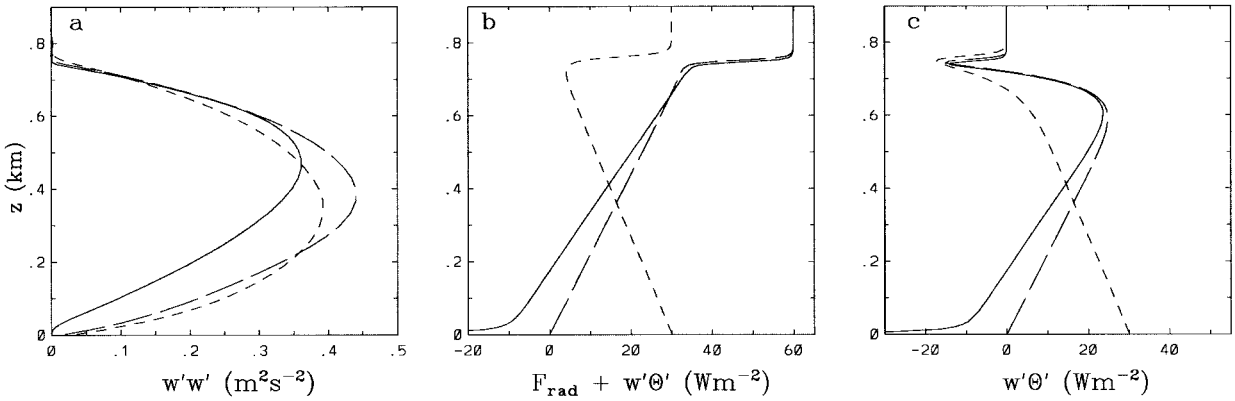

FIG. 10. Hour-averaged statistics from simulations of convectively driven boundary layers with different combinations of top and bottom fluxes: 91 (short dashes), 92 (solid), 12 (long dashes).

In Fig. 9 we compare results from this capped dry convection case with different horizontal resolutions (simulations 71–75), showing a modest variation in η_E with the entrainment flux generally dropping with increased resolution. We find that the buoyantly driven plumes are generally smaller (and the vertical velocity more skewed) in the surface-driven case than in the radiatively top-cooled boundary layer, so it is perhaps not surprising to see somewhat more sensitivity to horizontal resolution in this case. Nonetheless, given the order of magnitude range of horizontal resolution covered, the entrainment efficiency is still found to be remarkably robust. This agrees with the earlier observation (based on LES results) of Mason (1989).

Viewed as a boundary layer–scale process there are three steps to entrainment: the capture of warm fluid into the large eddy at the top of the boundary layer, the transport by the large eddy through the boundary layer, and finally the small-scale mixing throughout. In simulation 82 we again test, in somewhat different fashion, the sensitivity of the entrainment rate to the first of these processes. We again include a negative heat flux through the top lid (more than the dynamics can entrain) but distribute part of this flux in an exponential tail stretching 25 m below the top lid. Thus a portion of the heat input at the domain top is now into fluid at nearly the same temperature as the bulk of the boundary layer, and might be expected, therefore, to be more easily captured by the boundary layer–scale eddies. The entrainment efficiency is not significantly changed, however, suggesting that the energetics of large-scale-eddy transport has more to do with determining the entrainment rate than the capture efficiency through the inversion.

This conclusion is reinforced by the results of simulations 83 and 84. Simulation 83 has a low Reynolds number, showing again a marked decrease in entrainment efficiency relative to simulation 73 (at the same horizontal resolution). Simulation 84 also has a low Reynolds number but with the imposed top negative heat flux again distributed exponentially, stretching down now 50 m below the top lid. Again the entrainment efficiency is reduced relative to the high Reynolds number case, suggesting that the reduction in entrainment efficiency with low Reynolds number is due to changes in the large-eddy energetics within the boundary layer rather than a change in capture efficiency of the warm fluid below the inversion.

c. Hybrid dry convection

We conclude our dry convection simulations with two hybrid radiation–surface heat flux cases (Fig. 10). In the first, simulation 91, we include 30 W m^{-2} radiative cooling at the top of the smoke cloud and 30 W m^{-2} heat flux at the surface. A priori one might expect the entrainment efficiency to be midway between the cases driven with 60 W m^{-2} purely from the boundary layer top or bottom. Instead this efficiency is slightly higher than either of these. The inversion gradient is less sharp than in the purely top-driven case, increasing the direct cooling contribution to entrainment as well as the relative uncertainty involved in removing it from the large-eddy entrainment efficiency. Discounting this difficulty, the larger efficiency suggests that the more evenly distributed buoyancy flux in this case allows a more effective channeling of energy into driving the boundary layer–scale eddies, and a relative reduction in the dissipation.

In simulation 92 the dynamics are driven by radiative cooling as in the standard smoke case, but we include a negative surface heat flux, in analogy to the negative heat flux through the top lid in some of the bottom-driven simulations. Just as in these latter cases, we find that if the surface negative heat flux is sufficiently small it is all entrained into the boundary layer, but there exists a maximum value that can be entrained and any negative surface flux beyond this value serves only to cool a thin layer at the surface. In this case, then, we have entrainment at both the top and bottom of the boundary layer. We can compute an η_E for these independently, or for

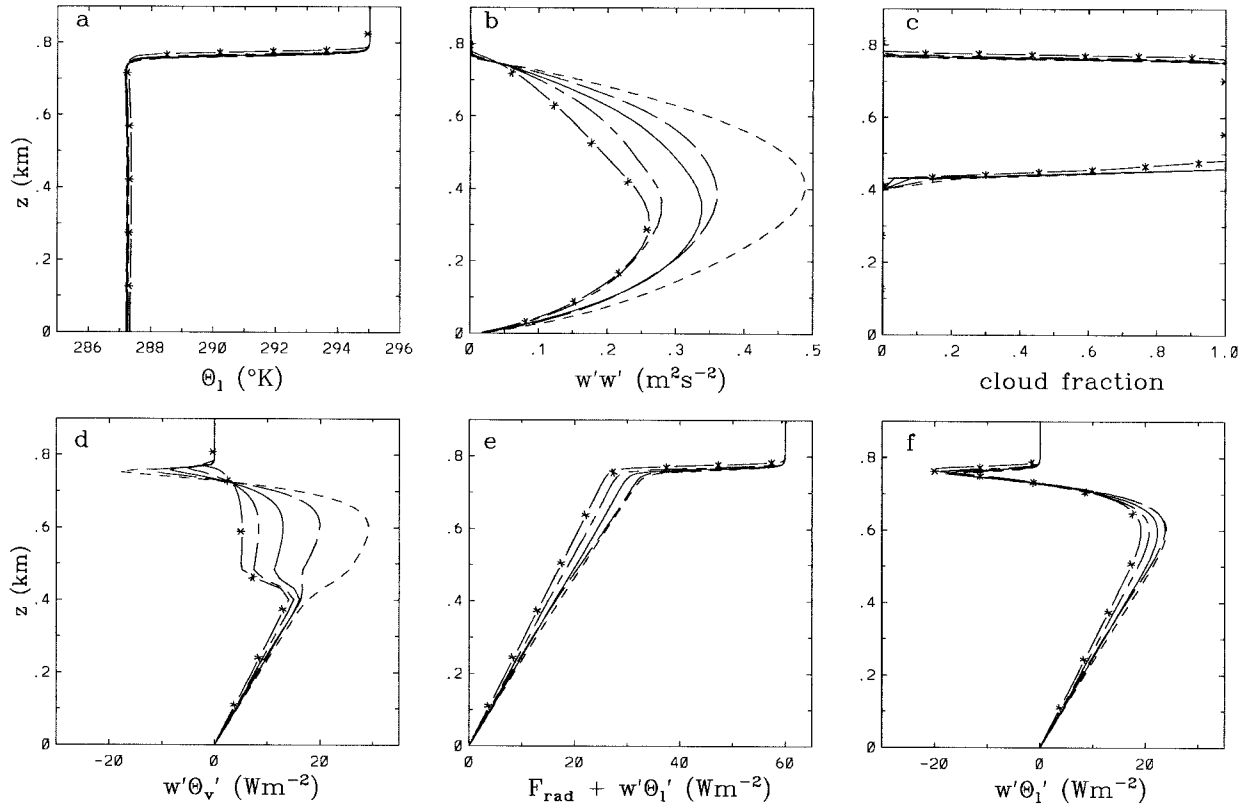

FIG. 11. Influence of different values of L/c_p on hour-averaged, mean statistics from simulations of a radiatively cooled, cloud-top boundary layer. Values of L/c_p = 0, 1000, 2450, 5000, 10 000 (simulations 116, 117, 112, 118, 119 respectively) indicated by dash patterns from high to low buoyancy flux in (d). (a) Liquid potential temperature, (b) total vertical velocity variance, (c) partial cloud fraction, (e) total thermal flux, and (f) total liquid potential temperature flux.

the combination. We find that it is the individual top and bottom entrainment efficiencies that have values comparable to those we have been considering (0.36 and 0.33, respectively). This is one of the few instances in which our results conflict with the suggested entrainment closure of Stage and Businger (1981a,b), who proposed that it is the combination of top and bottom entrainment cost that should be a constant fraction of the total available energy production. One possible explanation is that one leg of the boundary layer–scale eddy dynamics dominantly controls the entrainment rate (e.g., the downdrafts for entrainment at the boundary layer top and updrafts for entrainment at the bottom); the top and bottom entrainment dynamics would then inhibit each other only very little.

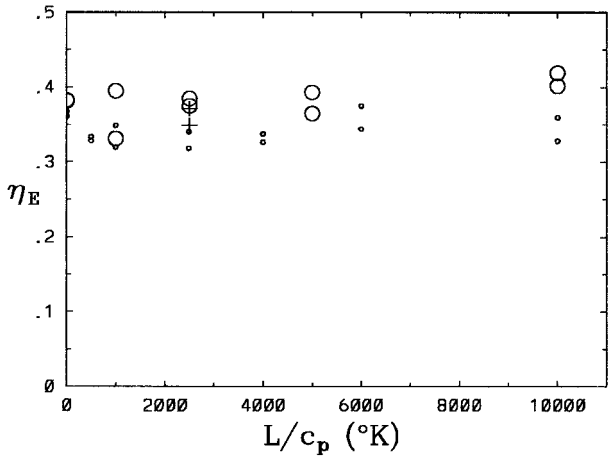

FIG. 12. Hour-averaged entrainment efficiencies as a function of the ratio of latent heat to specific heat for radiatively cooled, cloud-top boundary layers. Symbols indicate horizontal resolution: Δx = 50 m (+), 80 m (large circles), 160 m (small circles).

5. Simulations including liquid water dynamics

We turn now to boundary layer dynamics including evaporation and condensation effects. Many new complications arise over the dry convection cases already considered. There are now two entrainment fluxes that can enter into the dynamics (θ_l and q); the possibility for significant intermediate scale (in this case cloud scale) eddies; the possibility of an evaporatively unstable cloud top; and in general a decidedly nonlinear vertical buoyancy flux profile even in the limit of a sharp inversion and sharp cooling layer. For simplicity we

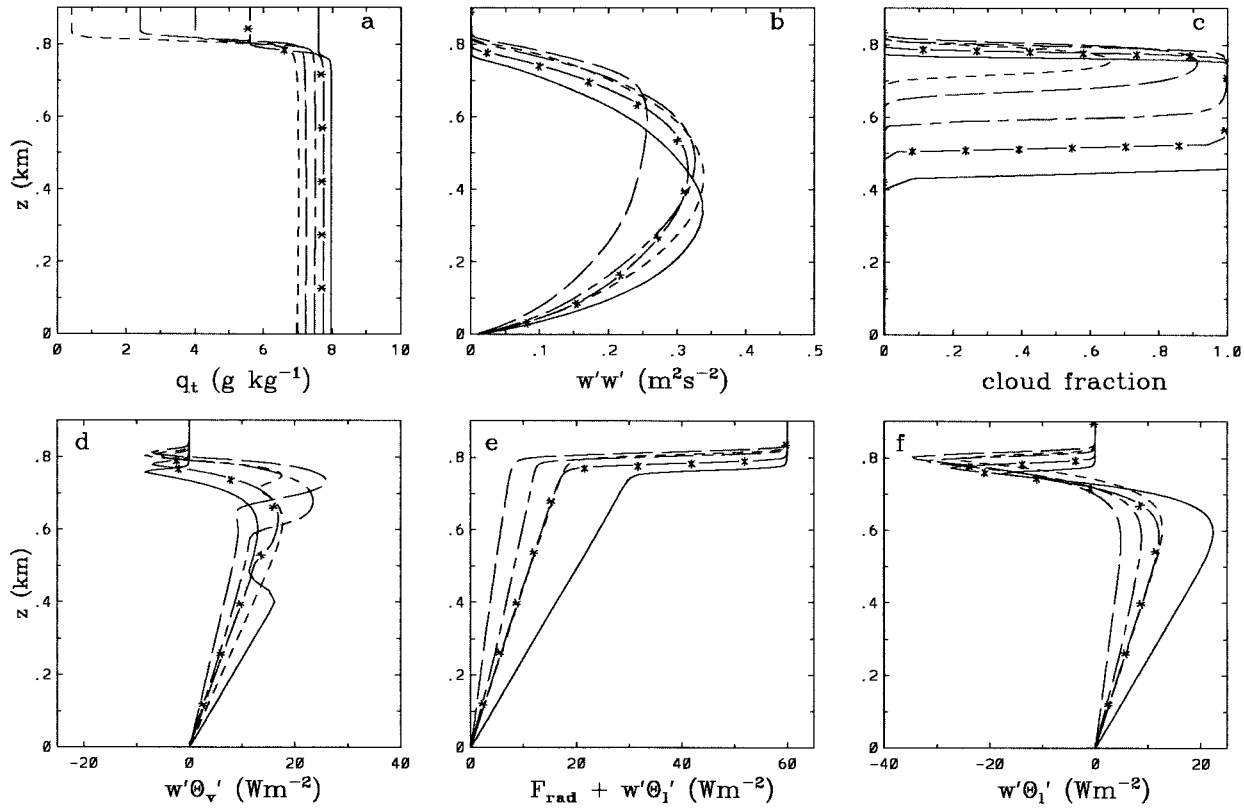

FIG. 13. Influence of different values of humidity jump at the inversion on hour-averaged, mean statistics from simulations of a radiatively cooled, cloud-top boundary layer (112, 122, 124, 126, 127 indicated by solid, starred, long–short-, long-, and short-dashed lines, respectively). (a) Total water mixing ratio indicating the dash patterns for different humidity jumps. (b)–(f) As in Fig. 12.

consider first a series of simulations in which only the last of these complications is significant.

a. Influence of varying L/c_p

We begin with the flow fields and concentrations from the standard smoke cloud case at the 2-h point, scaling the smoke concentration to a total water mixing ratio of approximately 8 g kg^{-1} in the boundary layer and only slightly smaller (7.6 g kg^{-1}) above the inversion, so that the total water flux due to entrainment will be small and have little effect on the dynamics. We maintain the same (constant) cooling rate and optical depth by tying the radiative cooling to the jump in the total water profile instead of to the liquid water profile. The case differs from the radiative smoke cloud only in the effects of liquid water on the buoyancy flux, and we vary this by changing the latent heat to specific heat ratio (L/c_p) employed within our LES model. The precise nature of how this varies the condensation dynamics is unimportant to the entrainment dynamics; the effect is solely through the buoyancy flux. Thus we may consider the variation to be in the shape of the buoyancy flux profile with the particular L/c_p variation used as a convenient artifice to achieve this. In the limit of L/c_p approaching zero we nearly regain the smoke cloud case, the difference being due to the change of θ_v arising from the density differences between dry air, water vapor, and liquid water (it turns out that L/c_p of approximately 500 reproduces the smoke case buoyancy flux).

Results for these simulations are given in Table A2 (110–119) and Figs. 11 and 12. Simulations 110 and 112 represent the physical case of $L/c_p = 2450$ in the boundary layer atmosphere. This series of simulations varying L/c_p is a clear case in which the parameterization in (1) suggests quite different results from those in (6), (7), and (8). As L/c_p is increased, the excess buoyancy of an entrained parcel is greatly reduced because as warm air from above the inversion is mixed into the cloud top it is cooled to an ever-increasing degree by cloud evaporation. The buoyant energy production from the radiative cooling is only modestly decreased. Within the cloud a fraction of the cooling goes to increase the liquid water mixing ratio, q_l, at the expense of a further decrease in θ_v, but below cloud base the change in L/c_p has no effect. The large-eddy entrainment cost for a given entrainment flux [as defined by the numerator in (1b)] is decreased by the same modest factor as the buoyant production for analogous reasons: within the cloud the negative buoyancy flux from the entrained temperature flux is partly offset by cooling from evap-

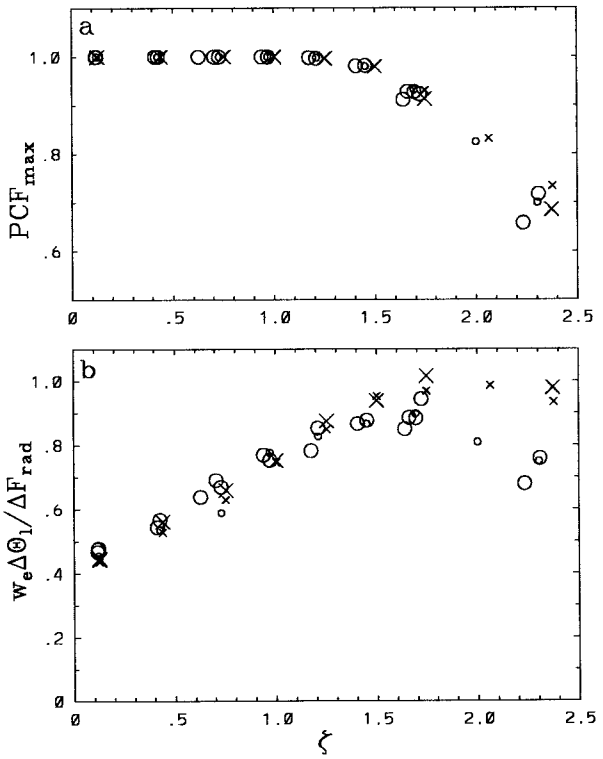

FIG. 14. (a) Hour-averaged maximum cloud fraction as a function of cloud-top stability [$\zeta \equiv (-L/c_p)(\Delta q_t/\Delta\theta_l)$] for radiatively cooled, cloud-top boundary layers. (b) Total entrainment flux normalized by total radiation flux jump as a function of cloud-top stability. The 1–2-h results are indicated by large crosses ($\Delta x = 50$ m or 80 m) or small crosses ($\Delta x = 160$ m); 2–3- and 3–4-h results are indicated by large circles ($\Delta x = 50$ m or 80 m) or small circles ($\Delta x = 160$ m).

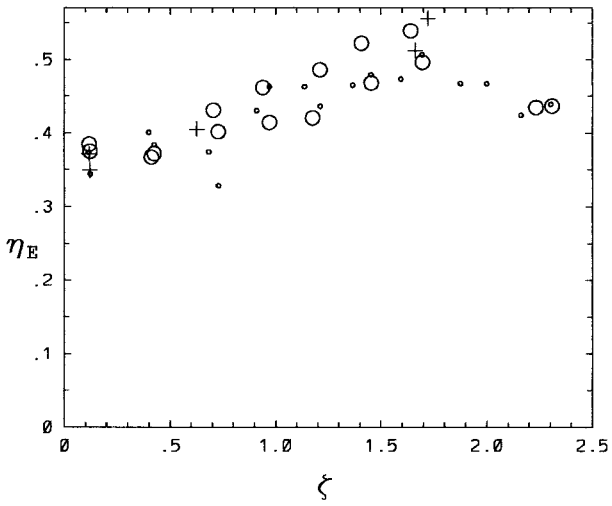

FIG. 15. Hour-averaged entrainment efficiencies as a function of cloud-top stability for radiatively cooled, cloud-top boundary layers as measured by ζ. Symbols indicate horizontal resolution: $\Delta x = 50$ m (+), 80 m (large circles), and 160 m (small circles).

oration within the cloud, but there is no change below cloud base. We would expect, then, a dramatic increase in entrainment flux with increasing L/c_p if small-scale mixing at the cloud top limits the entrainment rate, but little or no change if large-eddy transport is the limiting step setting the rate. The constancy of the measured entrainment efficiencies in Table A2 and Fig. 12 clearly support the latter scenario. The results in Fig. 12 also show, once again, a relative insensitivity to the horizontal grid resolution used in the simulation.

b. Influence of cloud-top stability

In simulations 110, 112, and 121–129, we leave L/c_p at its physical value and instead vary the humidity jump at the inversion. Other features of the simulations are as above. Sample vertical profiles of hour-averaged horizontal mean quantities are given in Fig. 13. As Δq_t is increased the cloud top becomes increasingly less stable and eventually unstable due to cloud-top evaporative cooling. At this point, the maximum partial cloud fraction (PCF) falls below 100% and the cloud is progressively eaten away by evaporation. In these latter cases the simulation results evolve significantly more in time, and quasi-steady statistics are more difficult to gather. We improve this situation considerably by again tying the radiative cooling to the total water profile rather than the liquid water content; thus the radiative cooling rate driving the dynamics remains fixed even as the cloud fraction or liquid water density at cloud top evolve. This cloud with fixed cooling deviates from the physical cloud ever more as the cloud fraction is reduced; accordingly we avoid small cloud fractions in these simulations. This simplification also eliminates any cloud-base radiative heating from the ground, which would directly drive cloud-scale eddies.

We can parameterize the cloud-top stability by the jump ratio $\zeta \equiv (-L/c_p)(\Delta q_t/\Delta\theta_l)$. We expect the cloud top to become nominally unstable for $\zeta > 4/3$ (Randall 1980; Deardorff 1980). We indeed find qualitatively different behavior above and below this point. When $\zeta < 4/3$, boundary layer scale eddies dominate the dynamics; the maximum partial cloud fraction remains 100%; the cloud water content slowly grows in time; the total entrainment increases linearly (Fig. 14); and the entrainment efficiency defined as in (1) remains fairly constant at a value consistent with that found above in the L/c_p variation (Fig. 15). As ζ increases above four-thirds the evaporation below cloud top and condensation above cloud base (i.e., the liquid water flux contribution to the buoyancy flux) dominates the energy production, driving significant cloud-scale eddies; the maximum partial cloud fraction drops below 100%; the cloud water decreases with time; the total entrainment levels off; and the entrainment efficiency as measured in (1) is enhanced.

Here we have realized the scenario described in section 2 in which smaller-scale eddies directly affect the

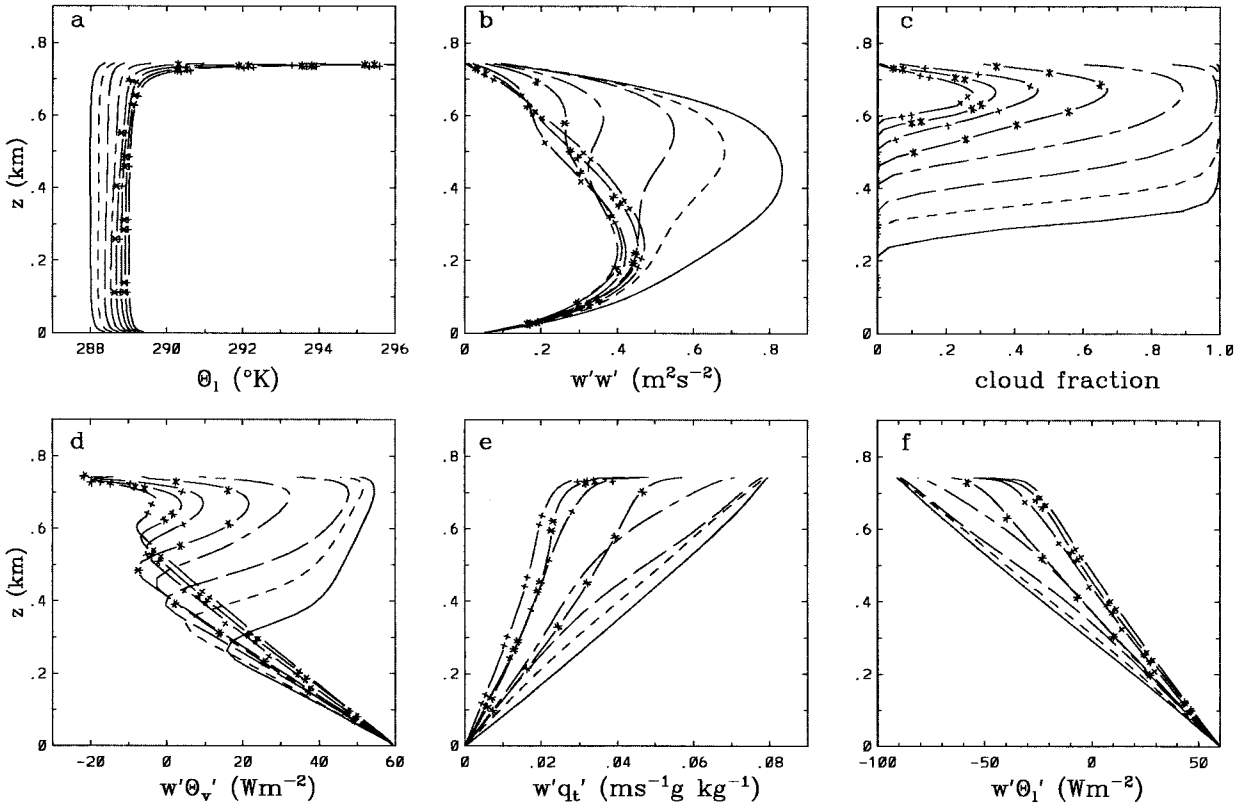

FIG. 16. Illustration of the time variation in simulation 182 with unstable cloud-top conditions; half-hour averages shown every one-half hour for a 4-h simulation progressing from thick to thin cloud layer.

energetics driving the large-scale eddies. The cloud-scale eddies mix some of the radiatively cooled air with some of the warm entrained air thereby reducing the amount of negatively buoyant fluid that is available to drive the boundary layer–scale eddies. The effect on the boundary layer–scale eddies is analogous to the loss of buoyant energy production due to the direct radiative cooling of warm inversion layer air. In this case we do not have a simple measure to diagnose what fraction of the radiative cooling is prevented from driving large-scale eddies in this fashion. We cannot, then, simply compute the large-eddy entrainment efficiency; it is overestimated in the way we apply (1) to get the results given in Table A2. Fortunately in this case a simpler entrainment limit tends to prevail. There is a maximal entrainment rate for which the entrainment heating rate equals the radiative cooling rate (indicated by a value of 1.0 on the *y* axis in Fig. 14b). Above this point there is no negatively buoyant fluid at cloud base left to drive boundary layer circulations and so the cloud layer decouples from the below cloud layer. If the evaporative instability at cloud top is strong enough relative to the radiative cooling this will happen, but it tends not to do so in our simulations. Decoupling at cloud base would shut off the humidity flux from below, which is responsible for much of the liquid water flux driving the dynamics in the cloud (as well as the entrainment); furthermore the cloud then dries out at a faster rate, decreasing the cloud fraction and therefore the rate of evaporative energy production (again decreasing the entrainment). For an unstable cloud top (but with the radiative cooling still dominating the dynamics), we find then, that the entrainment rate tends to remain just slightly below this maximal level as evidenced by the nearly zero buoyancy and thermal fluxes below cloud base seen in Fig. 13 for these cases and the plateau in total entrainment in Fig. 14.

In these simulations the cloud is initially solid and of order 200 m thick. As long as the cloud fraction remains close to one, we find the entrainment in the cases with unstable cloud top to be very nearly maximal. Later during the evolution, as the cloud fraction falls significantly below 100%, the entrainment falls off somewhat, to roughly three-fourths of the maximal level (Fig. 14). It is interesting to note that in this regime, when a quasi-steady cloud fraction has been achieved, the entrainment efficiencies measured via (1) are systematically larger than their counterparts in the case of a stable cloud top, but not grossly so. We thus have both a practical upper and lower bound on the entrainment in these cases. The integrated buoyancy flux is also found to be roughly constant in this region as ζ is increased, even though

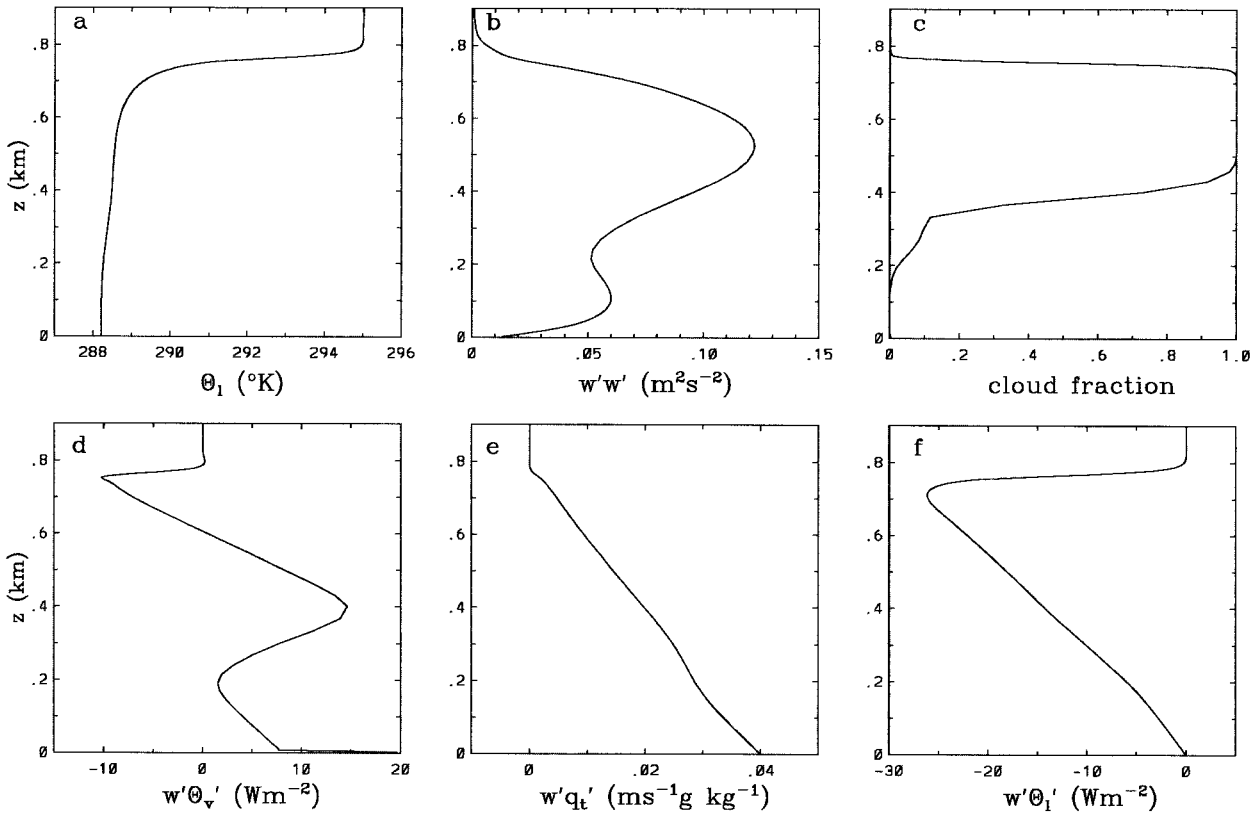

FIG. 17. Hour-averaged, mean statistics from simulation 192 of a cloud-top boundary layer driven by latent heat from the surface.

its vertical profile changes shape dramatically. The liquid water flux contribution within the cloud grows as the buoyancy flux below cloud base drops. Consistent results are again found for different horizontal resolutions, though the time variations within these runs necessarily makes the comparison less precise.

c. Hybrid cloud cases

Simulations 170–192 are further variations of cloudy boundary layers. In 170 and 171 a surface heat flux is added along with the radiative cooling. The cloud top is in the stable regime and the entrainment efficiencies are consistent with previous results. In simulations 181–183 we return to surface-driven convection with the boundary layer capped by a fixed lid with specified fluxes through it. As the domain heats up the cloud would naturally evaporate away; to prevent this we uniformly cool the domain to roughly balance the surface and entraining heat fluxes. Since the cooling is uniformly distributed it produces no dynamics directly. In simulation 181 we force a negative temperature flux through the top lid (more than can be entrained) but no humidity flux. This represents the limit of a tightly capped boundary layer with no Δq_t jump across the inversion. The entrainment efficiencies in Table A2 are consistent both with the case of surface-driven convection with no cloud (e.g., 71) and with the radiatively cooled cloud with a stable cloud top.

In simulation 182 we add a positive humidity flux through the top lid (i.e., entrainment leads to drying). The ratio of humidity flux to temperature flux employed corresponds to $\zeta = 2.5$—that is, an unstable cloud top. Horizontal mean, half-hour time averages of some vertical profiles are given in Fig. 16, progressing over 4 h of simulation. Given the strong time dependence we cannot gather precise entrainment measurements; we use this run instead to qualitatively illustrate the different entrainment regimes encountered when strong eddies are driven on different length scales. For the first hour shown the cloud is thick and solid. The cloud-scale eddies driven by evaporation, and the boundary layer–scale eddies driven by surface heating easily mix throughout the domain all of the flux we have imposed at the domain top. The buoyancy flux is everywhere positive and the temperature flux linear. During the next hour and a half, as the cloud thickness diminishes and cloud fraction falls below one, the cloud-scale eddies still easily mix all of the imposed top flux throughout the cloud layer (indeed are driven by it) but the surface-driven boundary layer–scale eddies now cannot keep up in their task of carrying this flux below cloud base. The buoyancy flux becomes negative around cloud base, and the temperature flux nonlinear. During this period the

cloud layer acts much like a thick inversion region, and the rate of entrainment of this fluid into the rest of the boundary layer is limited by the dynamics of the surface-driven boundary layer–scale eddies. Finally, toward the end of this simulated period, the cloud fraction continues to drop until the evaporatively driven cloud-scale eddies no longer entrain all of the imposed flux at the domain top. The entrainment rate is eventually governed, even in the cloud layer, by the surface-driven eddies, and the temperature flux is restored to linear. In the middle to late portion of this simulation, we encounter a maximal entrainment rate analogous to that found in the cloud-top cooled, evaporatively unstable simulation discussed previously. When the cloud top is unstable but the overall boundary layer dynamics are dominated by surface heating, the entrainment rate tends toward the maximum for which the cloud and below cloud layers can remain coupled. Decoupling is inhibited for the same reasons as in the top-cooled case.

In simulation 183 we add a constant moistening term to the simulation above so that a quasi-steady state can be achieved. The overall entrainment efficiency is consistent with the other cloud simulations. The efficiency computed for the below cloud dynamics alone is of order 0.2—that is, below but not far from the maximum of approximately 0.3, which can be sustained by the dry convective dynamics below cloud base. It is known that the approximation given in (4) for the coefficients relating the temperature and humidity fluxes to the buoyancy flux begins to break down as the boundary layer circulations become more highly skewed and the cloud fraction becomes small (e.g., Lewellen and Yoh 1993). This was not the case for the top-driven simulations considered above, but is a matter of concern in simulation 183. We can check the validity of (4) somewhat by comparing the integral of the measured buoyancy flux to that computed from the measured temperature and humidity flux profiles using (4). These integrals agree to within a few percent or better for all of the cases considered above except 183, for which the approximation underestimates the measured integral by 20%. As latent heat release becomes a large component of the total buoyant forcing we expect more of the fluxes to be carried in cloudy regions—in other words the effective r in (4) should be larger than the mean cloud fraction. In computing η_E for simulation 183 (and 192 below), we have improved upon this approximation as follows. We compute the integrated no-entrainment buoyancy flux two ways—first using the measured partial cloud fraction in (4) and second setting $r = 1$ whenever the measured cloud fraction is nonzero. We linearly interpolate between these results, with the fraction chosen as that which gives the measured buoyancy flux when the procedure is applied using the measured temperature and humidity fluxes. For simulation 183 this reduces the value computed for η_E using the mean cloud fraction by about 15%.

In our final case we touch upon dynamics where the buoyancy flux modeling becomes even more troublesome. In simulation 192 we drive the boundary layer dynamics purely through a surface moisture flux. Across the strong capping inversion the total water jump is small during that portion of the simulation for which we gather statistics. Thus the cloud top is very stable. To a good approximation, the only significant entrainment flux is that of temperature, while the only flux in the no-entrainment limit is that of humidity. Sample mean vertical profiles are given in Fig. 17. It is clear from the buoyancy flux profile that a measure of the entrainment efficiency based on, for example, (6), (7), or (8), would be very large. The ''A'' in (8), for example, is 13.7 for the hour average shown, about a factor of 50 bigger than the typical dry convection value. The combination $A/(A + 0.8)$ (which is more directly comparable to η_E) is 0.94 (vs 0.29 for simulation 70). On the other hand $\eta_E \approx 0.6$, which is larger than the values we have seen for other simulations with stable cloud tops, but only by about a factor of 2. There is some uncertainty in this value given the difficulty in estimating X_1 and X_2 for this case. We postpone a more detailed discussion of the surface latent heat flux case to a future paper, but offer two possible explanations for the relatively large value of η_E encountered here. The boundary layer dynamics driven by a surface latent heat flux differs markedly from that driven via sensible heat (Lewellen et al. 1996). The vertical velocity is highly skewed, the fluxes strongly correlated with the cloudy regions, and the temperature and humidity profiles are less well mixed. The dissipation dynamics is likely different as well and we would expect this to affect the entrainment efficiency. Perhaps more importantly, given the degree of stability that appears in the temperature profile at cloud base, there is a sense in which we have both top and bottom entrainment as in simulation 92, where the total entrainment efficiency (combining top and bottom) was found to be comparably large.

6. Conclusions and comments

The results of large-eddy simulations of quasi-steady, buoyantly driven, boundary layers that we have presented in this work, strongly support the conclusion that boundary layer–scale dynamics determines the entrainment rate, at least within some physical regimes. Within these simulations we have found the turbulent entrainment rate to be relatively insensitive to numerical or physical alterations that affect the small-scale mixing dynamics near the inversion but leave the boundary layer–scale eddy dynamics largely unchanged (e.g., changes in grid resolution, subgrid modeling, or modest wind shear). The entrainment rate is sensitive to changes that affect the large-scale dissipation dynamics (e.g., low Reynolds number) as one might expect given that entrainment and dissipation are the two competing energy sinks in these systems. Experiments with a lid in which we effectively attempted to impose larger

amounts of entrained heat flux provided additional evidence that the large eddies were controlling entrainment in our simulations: the large eddies could not mix the extra heat flux into the boundary layer, letting it accumulate at the domain top. These results do not rule out the existence of physical regimes in which small-scale mixing limits the entrainment rate; we can at best determine what governs the entrainment within the parameter space accessible to our simulations.

The most basic measure of entrainment dynamics from a boundary layer–scale eddy perspective is a global energetic one. Accordingly, we have defined a large-eddy entrainment efficiency, η_E, as the fraction of buoyant energy production available to drive large eddies that is lost to entrainment rather than dissipation. As we have implemented it, η_E is similar (but not identical) to the flux partitioning measure of Stage and Businger (1981a,b). Since this measure of entrainment cost is a global one, its implementation requires knowledge of boundary layer properties such as cloud fraction and depth; on the other hand it allows us to avoid defining a buoyancy jump at z_i (as is required with the A/Ri parameterization), which requires making assumptions about mixing at cloud top. We have found η_E to be fairly constant for a wide range of buoyantly driven boundary layers with broadly similar large-eddy dynamics, with no apparent fundamental difference in entrainment between top- and bottom-driven, or dry versus cloudy, boundary layers. This efficiency increases from ≈ 0.3 for a surface-driven boundary layer with a stable top, to ≈ 0.35 for a top-driven boundary layer with a stable top, and up to 0.5 for a quasi-steady boundary layer with an unstable cloud top with the cloud fraction reduced below one. The observed increase in entrainment efficiency coincides with the large-eddy energetics centered progressively higher in the boundary layer and driven progressively more by the liquid water flux contribution to the buoyancy flux.

Further work is required in the case of boundary layer dynamics driven by cloud-top cooling before operational estimates of entrainment rates are practical. That portion of radiative cooling occurring within the warm inversion region itself is not available to drive large-eddy dynamics. This ''direct cooling'' represents entrainment that is effectively 100% efficient. In this work we have made no attempt at predicting this contribution to entrainment, confining ourselves to roughly diagnosing its value within a given simulation so that we could focus on the large-eddy entrainment dynamics alone. As many researchers have pointed out, however, it can represent a significant contribution to entrainment. Since the fraction of radiative cooling in this category ultimately depends on details of local temperature and humidity gradients, this direct cooling contribution is likely to depend upon the local small-scale dynamics as well as the large-scale dynamics.

In boundary layer dynamics driven dominantly by cloud-top cooling but with significant cloud-scale eddy dynamics (driven, e.g., by an evaporatively unstable cloud top), we find that the cloud-scale eddies can directly mix warm inversion region air with the radiatively cooled air, thereby reducing the energy available to drive boundary layer–scale eddies, in a somewhat analogous manner to the direct cooling entrainment. This is an example where the large-scale-eddy dynamics is affected by the smaller scale. Fortunately in this case there exists a practical limiting entrainment rate that is achieved over a range of cloud conditions in our simulations. This is the entrainment rate for which entrainment heating almost balances the cloud-top cooling. A higher entrainment can be achieved only at the cost of decoupling the cloud layer from the below cloud layer, cutting off the humidity flux from below cloud, which helps to drive the cloud-scale eddies. We find in our simulations that as time progresses the cloud-top instability is partly relieved by reducing the cloud fraction; the entrainment rate accordingly drops below maximal and approaches again that limit set by the large-eddy entrainment efficiency.

Entrainment in clouds with dynamics driven dominantly by surface latent heat flux have only briefly been touched upon. The entrainment efficiency in the case considered was relatively large, $\eta_E = 0.6$, compared with other buoyantly driven dynamics, but the difference is far less dramatic than implied by other entrainment measures. The dynamics in these cases tend to be highly skewed (in part because of the entrainment). We need a more accurate model relating the buoyancy flux to the conserved temperature and water fluxes in order to accurately compute η_E for such highly skewed dynamics. This case is further complicated because the entrainment itself significantly changes the nature of the boundary layer–scale dynamics.

We have restricted our attention in this work to tightly capped, buoyantly driven, quasi-steady boundary layers; new features can arise outside of these limits. In weakly capped layers buoyant plumes can penetrate through the inversion; the dynamics can be sensitive to the lapse rate above the inversion and the entrained mass flux could become important in addition to the entrained temperature and moisture fluxes. Buoyantly driven dynamics tend to be special in at least two regards. First, surface or cloud-top temperature fluxes tend to predominantly drive boundary layer–scale eddies; while wind shear, for example, often directly drive eddies of different scales more uniformly. Second, the entrainment cost to the dynamics itself is through a buoyancy flux. Our most limiting restriction, however, is considering only quasi-steady dynamics. Under strongly transient conditions, eddies of different length scales need not be in equilibrium with one another and there can effectively be different entrainment rates for different length scales—that is, a single entrainment rate may not be sufficient to describe the entrainment dynamics. The addition of other physical effects that occur in nature, such as in-cloud heating due to solar radiation or sub-

cloud cooling due to drizzle, are likely to make transient conditions more prevalent. Some important boundary layer phenomena such as decoupling, or the breakup of a cloud layer due to cloud-top entrainment instability, are inherently transient in nature. In such cases it is important to consider the large-scale physics that drives the transient conditions and allows instabilities to arise; the future history of an instability cannot likely be divorced from its origins.

Finally we have not addressed in this work the actual mechanics of the large-eddy transport of entrained fluxes. What balance in particular sets the large-eddy entrainment efficiency, and why are entrainment results as robust as they are? The artifice of introducing a top lid with controlled fluxes through it may prove useful in understanding the underlying dynamics by allowing a more direct entrainment versus no entrainment comparison. It could prove useful in obtaining better statistics in laboratory measurements of entrainment as well.

Acknowledgments. This work was supported by a grant from the Office of Naval Research with R. F. Abbey Jr., technical monitor. D. L. would like to acknowledge useful conversations with the participants of the 1995 GCCS boundary layer cloud working group meeting in De Bilt, the Netherlands, where some of the results in this work were first presented.

APPENDIX

Simulation Tables

TABLE A1. Entrainment statistics from hour averages of convectively driven dry boundary layers. The second column provides brief notes on each run; η_E is as defined in (1b); η_{Epr} is for the previous hour; $\Delta\mathcal{F}$ is the total thermal entrainment flux, D.c.f. the fraction arising from direct cooling, A_{Ri} is the A defined in (8); column 9 is the integral of the buoyancy flux, with the fraction resolved in the next column; the last column is the integral of the turbulent kinetic energy.

Run	Notes	Δx m	η_E	η_{Epr}	$\Delta\mathcal{F}$ W m^{-2}	D.c.f.	A_{Ri}	$\int w\theta_v$ °m^2 s^{-1}	$(\int w\theta_v)$r	$\int$TKE m^3 s^{-1}
10	GCSS	50	0.37	0.36	26.7	0.42	0.78	8.67	0.98	427
11	GCSS	32	0.38	0.36	27.1	0.42	0.81	8.51	0.99	378
12	GCSS-(4–5-h avg)	80	0.35	0.37	26	0.44	0.78	8.86	0.96	370
13	GCSS-(6–7-h avg)	80	0.37	0.38	26.7	0.42	0.82	8.77	0.97	389
14	GCSS	160	0.36	0.33	26.4	0.42	0.80	8.77	0.92	422
15	GCSS	320	0.37	0.36	26.9	0.42	0.81	8.55	0.77	405
16	GCSS	1D	0.09	0.09	10	0.58	0.18	13.82	0.00	175
21	$\Delta z = 1.25$	80	0.37	0.33	25.5	0.37	0.71	8.91	0.97	406
22	$\Delta z = 2.5$	80	0.36	0.36	25.5	0.40	0.74	8.94	0.97	398
23	$\Delta z = 10$	80	0.38	0.37	29.6	0.49	0.95	7.78	0.96	343
24	$\Delta z = 20$	80	0.36	0.39	31	0.59	1.04	7.35	0.96	311
31	Pr = 50	50	0.34	0.33	24.8	0.42	0.72	9.17	1.00	378
32	Pr = 50	160	0.37	0.38	27.3	0.43	0.82	8.48	1.00	404
33	$\Lambda_{max}/\Delta x = 0.2$	80	0.40	0.39	28.2	0.40	0.90	8.25	0.98	403
34	$\Lambda_{max}/\Delta x = 0.4$	80	0.33	0.33	25.1	0.44	0.69	9.20	0.94	382
35	Low Re	50	0.15	0.16	16.7	0.63	0.30	11.43	0.95	273
41	$\Delta z_c = 20$	80	0.36	0.39	19.1	0.05	0.46	10.41	0.97	428
42	$\Delta z_c = 40$	80	0.35	0.34	18	0.01	0.36	10.13	0.96	399
43	$\Delta z_c = 40$	50	0.32	0.31	16.7	0.05	0.30	10.58	0.98	449
44	$\Delta z_c = 80$	80	0.32	0.31	16.2	0.018	0.21	9.65	0.96	401
45	$\Delta z_c = 160$	80	0.31	0.31	14.6	0.00	0.02	7.96	0.95	317
46	$\Delta z_c = 160$	50	0.29	0.31	14	0.00	0.02	8.40	0.98	330
51	Ka = 0.007	80	0.36	0.37	18.5	0.36	0.60	6.91	0.98	385
52	Ka = 0.01	80	0.36	0.36	21.3	0.33	0.67	8.09	0.98	401
53	Ka = 0.03	80	0.36	0.41	29.1	0.50	0.89	8.93	0.96	383
61	$\Delta u = 1$ m s^{-1}	80	0.37	0.36	27.4	0.44	0.80	8.47	0.97	401
62	$\Delta u = 2$ m s^{-1}	80	0.35	0.38	26.6	0.45	0.79	8.79	0.97	397
63	$\Delta u = 4$ m s^{-1}	50	0.44	0.43	33.4	0.53	1.22	6.53	0.99	331
70	surf.-driven	50	0.29	0.30	17.2	0.00	0.33	13.53	0.91	321
71	surf.-driven w/lid	50	0.32	0.31	19.3	0.00		13.23	0.91	301
72	surf.-driven w/lid	32	0.29	0.29	17.4	0.00		13.87	0.94	319
73	surf.-driven w/lid	80	0.35	0.35	20.8	0.00		12.73	0.86	286
74	surf.-driven w/lid	160	0.39	0.38	23.4	0.00		11.85	0.75	287
75	surf.-driven w/lid	320	0.37	0.34	22.3	0.00		12.52	0.58	330
81	No entrainment	50	0.00	0.00	0.00	0.00		19.81	0.93	507
82	Dist top flux	50	0.32	0.31	19.5	0.00		12.92	0.91	294
83	sf, low Re	80	0.20	0.23	12.3	0.00		15.44	0.87	198
84	sf, low Re,dist	80	0.16	0.17	9.9	0.00		15.48	0.87	198
91	30 W m^{-2} top + bot	80	0.39	0.40	28.5	0.37	0.76	9.26	0.90	336
92	Surf.-cooled	50	0.58*	0.56	33.5	0.30	1.22	5.19	1.00	210

* Here η_E(top) = 0.36; η_E(bottom) = 0.33.

TABLE A2. Entrainment statistics from hour averages of convectively driven cloud-top boundary layers. Nomenclature is similar to Table 1 with additions; q_{top} is the total water mixing ratio above the inversion; $\zeta \equiv (-L/c_p)(\Delta q_t/\Delta\theta_l)$ is a measure of cloud-top stability; and the last column is the maximum cloud fraction at any height.

Run	Notes	Δx m	q_{top} g/kg	ζ	η_E	η_{Epr}	$\Delta\mathcal{F}$ W m^{-2}	D.c.f.	A_{Ri}	$\int w\theta_v$ °m^2 s^{-1}	$(\int w\theta_v)$r	$\int$TKE m^3 s^{-1}	PCF$_{max}$
110	cloud-top cooled	50	7.6	0.1	0.37	0.35	29.0	0.40	1.03	6.26	0.99	303	1
112	cloud-top cooled-hor.res	80	7.6	0.1	0.38	0.37	29.7	0.40	1.08	6.1	0.98	325	1
116	$L/cp = 0$	80	7.6	0	0.38	0.38	28.0	0.45	0.76	9.49	0.97	421	1
117	$L/cp = 1000$	80	7.6	0.1	0.39	0.33	28.6	0.40	0.92	7.41	0.97	337	1
118	$L/cp = 5000$	80	7.6	0.2	0.39	0.36	32.1	0.38	1.34	5.01	0.97	275	1
119	$L/cp = 10\,000$	80	7.6	0.5	0.4	0.42	33.8	0.36	1.54	4.29	0.98	285	1
121	Δq variation	80	6.6	0.4	0.37	0.37	34.8	0.41	1.21	6.24	0.97	332	1
122	Δq variation	80	5.6	0.7	0.43	0.4	43.6	0.35	1.66	5.8	0.97	301	1
123	Δq variation	80	4.6	0.9	0.46	0.41	47.5	0.31	1.85	5.83	0.97	307	1
124	Δq variation	80	4	1.2	0.42	0.49	47.8	0.32	1.72	6.47	0.96	322	1
125	Δq variation	80	3.2	1.4	0.52	0.47	54.0	0.31	2.27	5.45	0.96	283	0.98
126	Δq variation	80	2.4	1.6	0.54	0.5	53.5	0.33	2.31	5.31	0.95	273	0.91
127	Δq variation	80	0.4	2.2	0.43	0.44	42.7	0.35	1.33	7.2	0.95	365	0.66
128	Δq variation	50	6	0.6	0.41		39.6	0.36	1.44	5.96	0.98	296	1
129	Δq variation	50	2.5	1.7	0.51	0.56	55.3	0.32	2.82	5.54	0.97	222	0.93
170	60 W m^{-2} surf. flux	80	6.6	0.5	0.35	0.4	66.8	0.38	0.82	19.9	0.91	561	0.97
171	23 W m^{-2} surf. flux	80	6.6	0.4	0.36	0.33	48.1	0.36	1.01	11.2	0.95	538	1
181	Surf T + lid T flux	50		0	0.32	0.32	23.3	0.00		12.9	0.9	282	1
182	Surf T + lid T,H flux	50		2.5	0.4	0.41	33.9	0.00		12.2	0.89	285	0.31
183	Surf T + lid T,H flux	50		2.5	0.38	0.39	46.9	0.00		11.8	0.9	227	0.38
192	113 Wm^{-2} surf. latent	50		0.2	0.63	0.66	27.8	0.00	13.7	2.82	0.92	70	1

REFERENCES

Bretherton, C., and Coauthors, 1998: An intercomparison of radiatively-driven entrainment and turbulence in a smoke cloud, as simulated by different numerical models. *Quart. J. Roy. Meteor.*, in press.

Deardorff, J. W., 1980: Cloud top entrainment instability. *J. Atmos. Sci.*, **37,** 131–147.

Kraus, H., and E. Schaller, 1978: A note on the closure in Lilly-type inversion models. *Tellus*, **30,** 284–288.

Lewellen, D. C., W. S. Lewellen, and S. Yoh, 1996: Influence of Bowen ratio on boundary-layer cloud structure. *J. Atmos. Sci.*, **53,** 175–187.

Lewellen, W. S., and S. Yoh, 1993: Binormal model of ensemble partial cloudiness. *J. Atmos. Sci.*, **50,** 1228–1237.

Lilly, D. K., 1968: Models of cloud-topped mixed layers under a strong inversion. *Quart. J. Roy. Meteor. Soc.*, **94,** 292–309.

Lock, A. P., 1996: Entrainment in clear and cloudy boundary layers. Ph. D. thesis, University of Manchester Institute of Science and Technology, Manchester, United Kingdom, 202 pp.

MacVean, M. K., and P. J. Mason, 1990: Cloud-top entrainment instability through small-scale mixing and its parameterization in numerical models. *J. Atmos. Sci.*, **47,** 1012–1030.

Mason, P. J., 1989: Large eddy simulation of the convective atmospheric boundary layer. *J. Atmos. Sci.*, **46,** 1492–1516.

McEwan, A. D., and G. W. Paltridge, 1976: Radiatively driven thermal convection bounded by an inversion—A laboratory simulation of stratus clouds. *J. Geophys. Res.*, **81,** 1095–1102.

Mellor, G. L., 1977: The Gaussian cloud model relations. *J. Atmos. Sci.*, **34,** 356–358; Corrigendum, **34,** 1483–1484.

Moeng, C. H., and J. C. Wyngaard, 1984: Statistics of conservative scalars in the convective boundary layer. *J. Atmos. Sci.*, **41,** 3161–3169.

——, S. Shen, and D. A. Randall, 1992: Physical processes within the nocturnal stratus-topped boundary layer. *J. Atmos. Sci.*, **49,** 2384–2401.

Randall, D. A., 1980: Conditional instability of the first kind, upside-down. *J. Atmos. Sci.*, **37,** 125–130.

——, 1984: Buoyant production and consumption of turbulence kinetic energy in cloud-top mixed layers. *J. Atmos. Sci.*, **41,** 402–413.

Sayler, B. J., and R. E. Breidenthal, 1998: Laboratory simulations of radiatively induced entrainment in stratiform clouds. *J. Geophys. Res.*, **103,** 8827–8838.

Schmidt, H., and U. Schumann, 1989: Coherent structure of the convective boundary layer deduced from large-eddy simulation. *J. Fluid Mech.*, **200,** 511–562.

Schubert, W. H., 1976: Experiments with Lilly's cloud-top mixed layer model. *J. Atmos. Sci.*, **33,** 436–446.

Sommeria, G., and J. W. Deardorff, 1977: Subgrid-scale condensation in models of nonprecipitating clouds. *J. Atmos. Sci.*, **34,** 344–355.

Sorbjan, Z., 1996: Effects caused by varying the strength of the capping inversion based on a large eddy simulation model of the shear-free convective boundary layer, *J. Atmos. Sci.*, **53,** 2015–2024.

Stage, S., and J. Businger, 1981a: A model for entrainment into a cloud-topped marine boundary layer. Part I: Model description and application to a cold-air outbreak episode. *J. Atmos. Sci.*, **38,** 2213–2229.

——, and ——, 1981b: A model for entrainment into a cloud-topped marine boundary layer. Part II: Discussion of model behavior and comparison with other models. *J. Atmos. Sci.*, **38,** 2230–2242.

Stevens, D. E., and C. S. Bretherton, 1998: Effects of resolution on the simulation of stratocumulus entrainment. *Quart. J. Roy. Meteor. Soc.*, in press.

Sykes, R. I., and D. S. Henn, 1989: Large-eddy simulation of turbulent sheared convection. *J. Atmos. Sci.*, **46,** 1106–1118.

——, W. S. Lewellen, and D. S. Henn, 1990: Numerical simulation of the boundary layer eddy structure during the cold-air outbreak of GALE IOP-2. *Mon. Wea. Rev.*, **118,** 363–374.

Turner, J. S., 1973: *Buoyancy Effects in Fluids.* Cambridge University Press, 367 pp.